Scattering of Ocean Surfaces in Microwave Remote Sensing by Numerical Solutions of Maxwell Equations

by

Tai Qiao

A dissertation submitted in partial fulfillment
of the requirements for the degree of
Doctor of Philosophy
(Electrical Engineering)
in the University of Michigan
2018

Doctoral Committee:

Professor Leung Tsang, Chair
Professor Anthony Grbic
Professor Christopher Ruf
Professor Fawwaz T. Ulaby

Tai Qiao

qiaot@umich.edu

ORCID iD: 0000-0002-7363-7008

To my family,

With love and gratitude.

ACKNOWLEDGEMENTS

I would like to express my thanks to my PhD advisor Professor Leung Tsang, for my gratitude to him to share his knowledge with me. During the four years' PhD study, I have learned so much from him. One thing I have learned from him is his attitude towards research. He spends most of his time during the day on research. For him, the truth of science always comes first. Even on weekends and deep into the night, we sometimes receive his emails or calls about new ideas about research. This touched me so much especially considering the fact that he is about to retire. Another thing that impressed me about him is his ability to broaden research topics and his concentration on research. For a particular problem, he has always been able to point out the key point and propose new ideas to draw other people's attention. He treats everything carefully. He sometimes talks about his personal life to us. His way of carefully handling everything and fulfilling his duty perfectly have influenced me very much. One particular thing that I want to mention is that he is so good at teaching. Even for a difficult concept like electromagnetics, he is able to find a way to interpret to students easily. I really enjoy the time during his class, during which I am so focused. This has never happened to me ever since my undergraduate study.

Also, I would like to thank my other 3 PhD committee members: Professor Fawwaz T. Ulaby, Professor Christopher Ruf, and Professor Anthony Grbic. Professor Ualby, Professor Ruf and Professor Grbic are all world famous scientists in their own areas. It is my great pleasure to have them on my committee.

During my PhD study one of my major source of support was the National Aeronautics and Space Administration (NASA). For the study of ocean scattering problems, I have been able to collaborate with Dr. Simon Yueh from the Jet Propulsion Laboratory (JPL) and Dr. Douglas Vandemark from the University of New Hampshire, Frederic Nouguier and Bertrand Chapron from the Laboratoire d'Océanographie Spatiale, Institut Francais de Recherche pour lâ'Exploitation de la Mer in France. Without the help from distinguished scientists, I would not have finished.

The first 4 months of my PhD study was spent at the University of Washington in Seattle. Here I also want express my thanks to my friends, staff and professors back at the University of Washington.

I have also received many help from my group mates and lab mates. They are Wenmo Chang, Shaowu Huang, Xiaolan Xu, Shurun Tan, Huanting Huang, Jiyue Zhu, Mohammadreza Sanamzadeh, Weihui Zhu, Maryam Salim, Yanlei Du, Liujun Zhu. and for those RadLab-mates, just to name a few, Dr. Jiangfeng Wu, Dr. Yang Liu, Dr. Adib Nashashibi, Dr. Leland Pierce, Mostafa Zaky, Mohammad Mousavi, Mani Kashanianfard, Zhanni Wu, Xiuzhang Cai, Han Guo, Weitian Sheng, and Nikolaos Chiotellis. Many thanks will also go to the all the staff and professors in the Radiation Lab.

During my PhD study, I have been a GSI for Professor Brain Gilchrist. I have really learned so much interesting knowledge about link design which is quite different from my research.

Most of my research work is related to high performance computing. Flux facility at the University of Michigan and Stampede at XSESE are the major two computational resources for me. As I approach completion of my PhD study, I want to express my thanks to the staff at these two supercomputing centers.

And of course the people who I have spent most of life time with are my family: my father Shungao Qiao, my mother Shuping Jiang, and my older sister Yong Qiao. Without their love and support I could not finish this thesis. Also I want to thank my paternal grandparents who are now both over 80. Now they live peacefully in a small countryside home back in my hometown in Northern China.

Most of the past 4 years' time were spent at the University of Michigan, Ann Arbor. I really like the university and the city of Ann Arbor. I have many good memories in different places on the campus and the city of Ann Arbor. I wish one day I can come back to the university and work in it.

Tai Qiao

April, 2018

Ann Arbor

TABLE OF CONTENTS

LIST OF FIGURES

LIST OF TABLES

ABSTRACT

The purpose of this thesis is to study the nature of electromagnetic scattering by the sea surface using numerical methods.

Sea-surface scattering has long been studied using various analytical methods. These analytical methods include the two scale method (TSM), the small-slope approximation (SSA), the small-perturbation method (SPM), the Advanced Integral Equation Method (AIEM), and the Geometrical/Physical Optics (GO/PO) method. These analytical methods rely on making approximations and assumptions in the modelling process. Some of these assumptions undermine their applicability in a wide range of situations. The input for analytical methods are usually the ocean spectrum. In real implementations, there are 2 sources of uncertainty in such approaches: (1) the analytical methods have a limited range of applicability to the surface scattering problem; the approximations made in these methods are questionable and (2) the various ocean spectra are another source of uncertainty.

We earlier applied a numerical method in 3-dimensions (NMM3D) to the scattering problem of soil surfaces. Through comparison with measured data, we established the accuracy and applicability of NMM3D. We see a drastic increase of ocean remote sensing applications in recent years. It is thus feasible to extend NMM3D to the sea-surface scattering problem. Compared to soil, sea water has a much higher permittivity, e.g., $75+61i$ at L-band. The large permittivity dictates the need for using a much denser mesh for the sea surface. In addition, the root mean

square (rms) height of the sea surface is large under moderate to high ocean wind speeds, which requires a large simulation area to account for the influence of long scale wave like gravity waves.

Compared to the two-scale model commonly used for the ocean scattering problem, NMM3D does not need an ad-hoc split wavenumber in the ocean spectrum. Combined with a fast computational algorithm, it was shown that NMM3D can produce accurate results compared to measured data like the Aquarius missions. TSM could also match well with Aquarius provided with a pre-selected splitting wavenumber. But it was observed that the result of TSM changes with different splitting wavenumbers. It is seen that TSM is fairly heuristic while NMM3D can serve as an exact method for the scattering problem.

On the other hand, through our study of NMM3D, we found that with a fine grid, the final impedance matrix converges slowly and also it becomes hard to perform simulations for a large surface. This has provoked us to (1) solve low convergence problem for a dense mesh and (2) resolve difficulties in simulations of large surfaces.

Inspired by the existing impedance boundary condition (IBC) method, we proposed a neighborhood impedance boundary condition (NIBC) method to solve the slow convergence problem caused by the dense grid. Different from IBC where the surface electric field and the surface magnetic field are related locally, NIBC relates the surface electric field to the magnetic field within a preselected bandwidth BW. Through numerical simulations, we found that the condition number can be reduced using NIBC. Errors of NIBC are controllable through changing BW. We applied NIBC to various wind speeds and surface types and found NIBC to be quite accurate when surface currents only suffer an error norm of less than 1%.

On the other hand, in contrast to the large permittivity of sea water, the air permittivity is small and has a rather smooth green function. Utilizing the Steepest Descent Method (SDM), we

successfully combined the Fast-Fourier-Transform (FFT) with the Physics-Based Two Grid (PBTG) method. PBTG states that a dense grid is needed for a medium with a high dielectric constant while it is not necessary for air. Eventually, our analysis led to a dense grid, e.g., 64 points per wavelength for green function in the lower medium and a coarse grid, e.g., 8 points per wavelength for green function in air.

Utilizing NMM3D, the anisotropic property of ocean backscatter for different wind direction is studied using two different ocean spectra. It is concluded that at L band, the dominant scattering mechanism is Bragg scattering.

Chapter 1 Introduction

This thesis is dedicated to the study of microwave scattering by the sea surface using numerical methods.

Usually, sea-surface scattering is modeled by analytical methods like the Advanced Integral Equation Method (AIEM), the Small Slope Approximation (SSA), and the Two Scale Model (TSM), among others. These analytical models involve the use of approximations in the modeling process, and thus have a limited range of implementation. In contrast, the numerical method makes no approximations in the modeling process. Surface integral equations are derived from Maxwell equations directly and then solved by the moment method. The input to NMM3D is the real surface profile generated from the ocean spectrum. Unlike a soil surface, the sea surface has a large permittivity and across a large rms height. These two features of sea water and sea surface requires a fine grid up to 64 points per wavelength a large simulation area. A dense grid results in a slow convergence rate for the final impedance matrix equation and a large surface will bring the CPU and memory burdens for the computing clusters. The rest of the thesis will try to solve these problems.

1.1 Surface scattering of sea surfaces

Derived from Maxwell equations, the surface integral equations (SIE) are the governing equations for scattering problems. The unknowns are the surface electric fields and surface magnetic fields. In solving the surface integral equations using moment methods, Rao-Wilton-Glisson (RWG) functions have been used as the basis and testing functions. The ocean surface

profile is generated using linear method with an ocean spectrum. The used ocean spectrum is truncated with a lower limit and upper limit. The lower limit and upper limit are related to the surface length and surface discretization density. Then the surface profile is meshed into triangles where RWG functions can be applied.

In solving the final impedance matrix equation, the most computationally intensive part is the product of the matrix by a column vector. To expedite this process, we have implemented Sparse Matrix Canonical Grid (SMCG) method. This method is based on the Taylor expansion of Green function about the flat surface. We project the green function onto the flat surface, then a 2 dimensional fast fourier transform can be carried out. We also combine the RWG basis function with the SMCG method to achieve both accurate and fast computation. Since we are simulating a finite surface, tapered incidence wave have been used to avoid edge diffraction.

As an approximation to the relation between surface electric field and surface magnetic field, impedance boundary condition (IBC) has been used widely to surface scattering problem. Out findings are that IBC works fine for surface with a large radius of curvature and large permittivity. But for ocean surface, the capillary waves are the main contributor to backscattering. IBC is not so applicable.

We compared our NMM3D results with other analytical methods and also Aquarius measurement data. It is showing that both NMM3D and TSM can predict well matched backscatter with Aquarius. But TSM needs a pre-selected splitting wavenumber to dive the ocean spectrum into SPM part and GO/PO part. When we change the splitting wavenumber, the scattering coefficients produced by TSM will also change. The standard of selecting the splitting wavenumber is like data fitting to produce the best matching with data. Thus TSM is pretty heuristic and cannot be regarded as an exact solution to electromagnetic scattering problem.

1.2 Scattering of anisotropic ocean spectrum

At L band, a new puzzle observed from recent radar missions appeared. As a function of azimuthal dependence, upwind radar scattering cross sections at L band are generally observed to be larger than cross wind radar cross sections. However, at lower winds near 3-5 m/sec, a reversal has been observed where the cross wind radar cross section exceeds upwind. This phenomenon is labelled as a Negative Upwind-Crosswind (NUC) asymmetry. In this thesis we also try to find the reasons lead to NUC by NMM3D. Two candidate anisotropic spectra are explored in Chapter 3: 1) the Elfouhaily Spectrum with and without an imposed nonlinear horseshoe pattern; 2) the Apel Spectrum with an empirically-modified spreading function. The modified angular spreading function is obtained using the advanced integral equation EM scattering method (AIEM) and satellite measurements and where millimeter and centimeter waves crosswind are allowed to be stronger than that of the upwind/downwind. Simulation results show that horseshoe pattern do not cause NUC to happen while the new angular spreading function can reproduce NUC. This leads to the conclusion that at L band Bragg scattering dominate the backscattering.

1.3 Neighborhood impedance boundary condition (NIBC)

Through doing 3D scattering problem of sea surface using numerical method, some numerical problems arose. The sea water permittivity is very large compared to air. The wavelength in sea water is 8 times shorter than that in air at L band. This requests a dense mesh when preforming moment method to the surface of sea surface. However, a dense grid will create some significant numerical problem including slow convergence, large CPU and memory consumption.

Inspired by the usual Impedance Boundary Condition (IBC), we are thinking of relating the surface electric field with the surface magnetic field accurately. IBC relates local electric field

with local magnetic field. This means the local electric field is only related to the magnetic field at the same spot. This approximation is made for flat surface with an infinite permittivity. But the truth is surface electric field can be incited by anywhere resided magnetic field. But thanks to the highly lossy feature of sea water, local electric field are only influenced by a small range of magnetic fields that surround it. Thus we can use a band matrix to represent such a relationship.

We are testing the NIBC in 2D scattering problem. Results show that 1) the error of NIBC is controllable by changing the bandwidth we are using. 2) NIBC is applicable to a wind range of ocean winds conditions and various surface types. Compared to IBC, NIBC is more accurate in that the surface fields only have an error norm of less than 1%. More importantly, it is found that the resulted equation has a much condition number than the usual dual surface integral equation.

1.4 PBTG in conjunction with SMCG

For scattering of random rough surfaces, we have kept mentioning sparse matrix canonical grid (SMCG) as our fast method in moment method for accelerating matrix vector multiplication. And also dense grid should be used due to the large permittivity of sea water. But on the other hand, the permittivity of air is relatively small. So there is a need to use dense grid for green function in the sea water but not for the green function in the air. The goal of Chapter 5 is to achieve that dense grid used in sea water but coarse grid in the air. Similar concept has been proposed by Tsang during the 1990s and 2000s and is called Physics-Based Two-Grid Method (PBTG).

With the help of steepest descent method (SDM), a new equation is formulated and through which we have been able to combine Fast Fourier Transform (FFT) with PBTG. Finally, combined with NIBC, it is seen that green function in the sea water is discretized with dense grid, e.g., 64

points per free space wavelength which the air green function is discretized with coarse grid, e.g., 8 points per free space wavelength.

1.5 Overview of the thesis

The thesis focuses on numerical modeling of sea surface interaction with electromagnetic waves at L band. We compared the numerical results with other analytical method and studied an interesting phenomenon called Negative Upwind-Crosswind (NUC) Asymmetry for 3D problems. This is the first time that the numerical problems are used to compare to the measured data and used to study the NUC phenomenon [44].

For the fast algorithm, we have proposed Neighborhood Impedance Boundary Condition (NIBC) and combine SMCG and PBTG to accelerate computation speed and speed up the iteration rate. NIBC is proposed to solve the dense grid problem resulted by the large permittivity of sea water. The study of dense grid with more than 30 points per free wavelength is never reported in previous numerical models [47] [50].

The Aquarius data used in this thesis is provided by Dr. Simon Yueh from the Jet Propulsion Laboratory.

Chapter 2 Sea Surface Radar Scattering at L-Band Based on Numerical Solution of Maxwell's Equations in Three Dimensions (NMM3D)

2.1 Introduction

Physical models of electromagnetic scattering from random rough surfaces have broad applications in microwave remote sensing of land surfaces and ocean surfaces. Analytical approximate methods include the small perturbation method (SPM), Geometrical Optics (GO), Physical Optics (PO), Advanced Integral Equation Method (AIEM), the Small Slope Approximation (SSA) and the composite surface model [1-6].

Ocean surfaces have a range of scales, with gravity waves of order of meters and short gravity and gravity-capillary waves with scales in the range of centimeters to millimeters. A common scattering model is the composite surface model, also known as the two scale model (TSM) [7-8]. In this approach, the surface height spectrum is divided in two in order to separate large- and small-scale roughness elements. Physical/Geometrical optics and SPM are applied, respectively, to the two scales, and the total radar cross section is obtained by summing the two contributions. The dividing line is usually chosen to be a half of the free-space wavenumber of the incident microwave [9, 10]. The two-scale model is a heuristic model as the decomposition of an object into parts followed by coherently or incoherently combining the scattering of each does not follow from Maxwell equations, otherwise Maxwell equations can be readily solved for any large object. Thus TSM requires tuning of dividing line between large scales and small scales.

In recent years, numerical simulations of 3D rough surface scattering have become feasible by combining fast numerical methods and high performance computing [11-15]. The simulations

have been applied to land and ocean surfaces. Both land and sea surfaces have fine-scale (mm to m) features that can cause significant microwave radar backscattering. For example, gravity-capillary and capillary waves have small radii of curvature compared with microwave wavelength that can lead to strong backscattering and cross-polarized returns. Because of the fine scale surface features, the surface integral equation approach, with discretizations of surfaces, is more accurate than using the FDTD (Finite-Difference Time-Domain) or FEM (Finite Element Method) approaches. The latter two methods require volumetric discretization. The surface integral equation approach combines fine-scale surface discretization with the method of moment (MoM) to capture the impact of all relevant surface structure on the scattered electromagnetic radiation. Examples of fast dense matrix solvers include the sparse matrix canonical grid method (SMCG) [16] and the Multilevel Fast Multiple Algorithm (MLFMA) [12]. In order to reduce the number of iterations, a near-field preconditioner has been used [14]. Some past work in numerical simulation treated the ocean surface as a perfect electric conductor (PEC) [15]. Some have implemented impedance boundary conditions (IBC) [17, 41]. The impedance boundary condition states that the tangential electric field is equal to the product of the wave impedance of the ocean permittivity and the tangential magnetic field. The approximation is valid if the radius of curvature of the surface is large compared with the microwave wavelength. Compared to previous works which are making approximations in the modeling process, in this chapter Maxwell equations are solved with a finite permittivity. Some earlier works are simulating 1 dimensional surfaces or 2 dimensional surfaces with pulse basis functions, while in this work 2 dimensional surfaces with RWG basis functions are being studied [18-23].

In this chapter, we apply NMM3D (Numerical Maxwell Model in 3-D) [11] to simulate L-band radar scattering from a wind-roughened ocean. The surface integral equations of PMCHWT

(Poggio-Miller-Chang-Harrington-Wu-Tsai) [12] are used. The ocean surface profiles are stochastically generated using three dimensional ocean spectra. In PMCHWT formulation, two separate Green's functions are used, one for air permittivity and another for ocean permittivity. The Sparse Matrix Canonical Grid (SMCG) [16] is used in conjunction with RWG basis functions. For modeling of the rough surface scattering, the physical problem is 3D vector wave scattering. However, the rough surface boundary has 2 dimensions with 2 degrees of freedom. The SMCG method uses a Taylor expansion of the Green's function about the flat surface so that 2D Fast Fourier Transforms (FFT) can be applied to the 3D electromagnetic scattering problem. The SMCG method has been implemented in a parallel computation framework [24]. The scattering problems in this chapter include cases with up to 6 million surface unknowns in the tangential electric and magnetic fields. In NMM3D simulations, a finite surface size is used and the surfaces are discretized. This means that the ocean spectrum is truncated between k_l and k_u, where k_l is inversely proportional to the surface size while k_u is inversely proportional to the discretizing sampling. Note that in NMM3D simulations, there is no need to impose a surface scale separation within this domain of k_l to k_u. By changing k_l or surface size, one can investigate the influence of adding roughness due to longer ocean surfaces. By varying k_u, one can assess the impact of small scale capillary waves. This study will focus on L-band ocean backscattering simulations and their comparison to results obtained from the Aquarius satellite radar system for wind speeds of 5, 8 and 10 m/sec. Aquarius measurements provide estimates for VV, HH, VH, and the VV/HH ratio and NMM3D backscattering results are produced for each case. Comparisons will also be made with TSM backscatter estimates to evaluate the efficacy of this widely used approximation method.

The chapter is organized as follows. In section 2.2, we describe the ocean spectrum used in this study. In section 2.3, we describe the formulations of surface integral equation and the

numerical implementations. In section 2.4, the influences of k_l and k_u, the lower and upper limits of truncated ocean spectrum on backscatter are illustrated. In Section 2.5 we illustrate numerical results and make comparisons to data and the TSM model.

Also in this chapter, the Aquarius data is actually the results of geophysical model function (GMF). The GMF is the experimental formula that relates the backscatter with wind speeds and wind directions. The following is a typical definition of GMF

$$\sigma_{pq} = A(w,\phi)\left(1+A_1(w)\cos(\phi)+A_2(w)\cos(2\phi)\right) \tag{1}$$

In equation (1), σ is the backscatter. w is wind speed. ϕ is wind direction. A, A_1, A_2 are coefficients through data fitting with measurement data.

2.2 Ocean spectrum and surface generation

Ocean roughness spectra have been extensively used in electromagnetic modeling of ocean surface scattering. Common ocean spectra include the Pierson-Moskowitz, Durden-Vesecky [16, 26] (DV), Donelan-Banner-Jahne and Elfouhaily spectra [25, 27-29]. These wind-dependent ocean wave height models are written in the form of the product of an isotropic part and an azimuthal anisotropic (wave direction) part

$$W(k,\phi,u) = \frac{1}{k} S(k,u)\Phi(k,\phi,u) \tag{2}$$

$$\Phi(k,\phi,u) = 1+\Delta(k,u)\cos(2\phi) \tag{3}$$

where $S(k,u)$ is the omnidirectional spectrum with k being the spectral components and u being the surface wind speed. ϕ is the azimuthal angle with respect to the wind direction. $\Phi(k,\phi,u)$ is the directional spreading function or angular dependence function which denotes the nonuniform distribution of wave roughness in azimuth. In this chapter, we used Durden-Vesecky spectrum for

the NMM3D simulations. Appendix B gives the expression of the Durden Vesecky spectrum. Two versions are used. One version is the isotropic, or omnidirectional, spectrum defined by setting $\Delta(k,u)=0$, and is referred to as isotropic DV in this chapter. The other version used is the full directional DV spectrum, referred to as the anisotropic DV spectrum. Although other spectrum can be used such as the Elfouhaily spectrum, the purpose of this chapter is to use NMM3D simulations to compare with the results of TSM and small perturbation method. Thus we limit ourselves to the isotropic and anisotropic DV spectrum [26].

In this study, the microwave frequency is 1.26GHz, which is the frequency of the Aquarius L-band scatterometer. The wavenumber of the microwave k_0 is 26 m^{-1}. According to the Bragg scattering theory [29, 30], the spectral component of the ocean spectrum that contributes to the backward scattering is

$$k_B = 2k_0 \sin\theta \tag{4}$$

where for the incidence angle (θ) of 39°, the Bragg scattering wavenumber is 33 m^{-1}.

In the rough surface simulations computed using DV as input for the surface integral equation approach [15], we specify the surface area to be of an extent L_x and L_y in x and y directions respectively. We also set surface lengths $L_x = L_y = L$. In the discretization of the surfaces, sampling intervals of $\Delta x = \Delta y$ are used. These limits set surfaces that contain spectral components $W(k,\phi,u)$ in the range of $k_l \le k \le k_u$, where

$$k_u = \frac{\pi}{\Delta x} \tag{5}$$

$$k_l = \frac{2\pi}{L} \tag{6}$$

In Figure 1, we show a log-log scale of the isotropic Durden-Vesecky spectrum for wind speeds 5 m/s, 8 m/s, and 10 m/s. The wavenumber of the incident microwave, the Bragg wavenumber, k_l, k_u for several surface lengths and sampling are also shown. In Figure 1, the lower limit k_l corresponds to a surface by $64\lambda \times 64\lambda$ and the upper limit k_u corresponds to $\Delta x = \Delta y = 1/32\lambda$. The incident L-band and Bragg wavenumbers lie between the upper limit and lower spectral limits.

In Table I, we tabulate k_l and k_u values corresponding to the surface sizes and the discretization intervals used in this chapter. With the increase of surface length, large scale ocean waves are incrementally increased in the simulations. The peak wavenumber for 5 m/s, 8 m/s and 10 m/s are around 0.27m^{-1}, 0.1m^{-1}, and 0.07m^{-1}. With a limited surface simulated, not all scales of ocean waves are included in the simulation. The rms heights for wind speed 8m/s 10 m/s are not the same as real ocean surfaces.

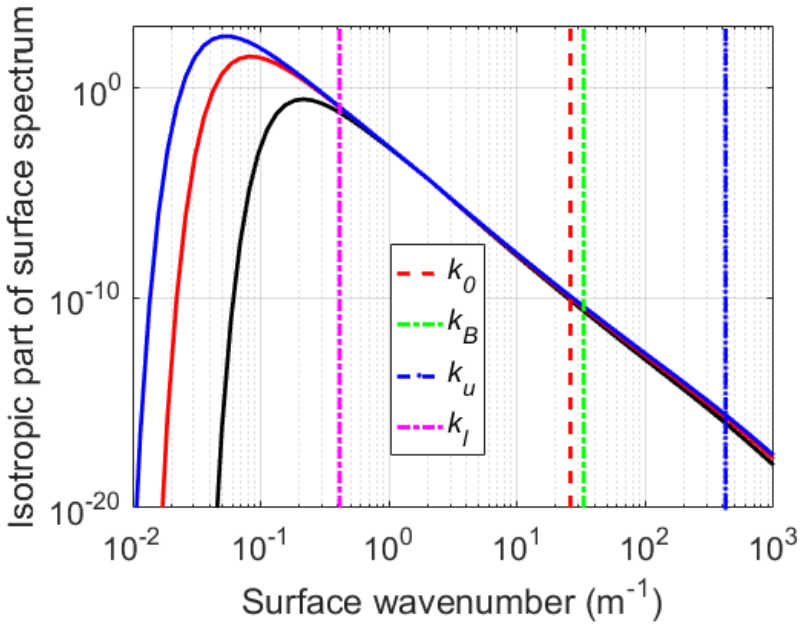

Figure 1 Isotropic Durden-Vesecky surface elevation spectrum (solid lines) for wind speeds 5 m/s, 8 m/s, and 10 m/s. Magenta and blue lines denote lower and caupper limit. The lower limit k_l corresponds to a surface size of $64\lambda \times 64\lambda$. Upper limit k_u corresponds to $\Delta x = \Delta y = 1/32\lambda$. Red

and green lines denote the incident microwave wavenumber and Bragg wavenumber respectively.

Table I Upper and lower spectral limits for varying sampling point densities and surface sizes

Surface Length (λ)	$\Delta x, \Delta y$ (λ)	k_l (m^{-1})	k_u (m^{-1})
16	1/16	1.65	211
32	1/16	0.82	211
16	1/32	1.65	422
64	1/16	0.41	211

2.3 PMCHWT surface integral equation and numerical implementation using RWG and SMCG

In this section, we summarize the methodology of NMM3D simulations [13-15].

For scattering by dielectric surfaces, the PMCHWT formulations of surface integral equations (SIE) are given in the following form:

$$\begin{bmatrix} -T - \frac{\eta_1}{\eta} T_1 & K + K_1 \\ -K - K_1 & -T - \frac{\eta}{\eta_1} T_1 \end{bmatrix} \begin{bmatrix} \tilde{J} \\ M \end{bmatrix} = \begin{bmatrix} \hat{n} \times \bar{E}^{inc} \\ \hat{n} \times \bar{H}^{inc} \end{bmatrix} \tag{7}$$

where

$$T_i(\mathbf{X}) = ik_i \hat{n} \times \int_S \left(\bar{\bar{I}} + \frac{\nabla\nabla}{k_i^2} g_i(\bar{r}, \bar{r}') \right) \cdot \mathbf{X}(\bar{r}') d\bar{r}' \tag{8}$$

$$K_i(\mathbf{X}) = \hat{n} \times P.V. \int_S \nabla g_i(\bar{r}, \bar{r}') \times \mathbf{X}(\bar{r}') d\bar{r}' \tag{9}$$

and

$$g_i\left(\bar{r},\bar{r}'\right)=\frac{e^{ik_i\left|\bar{r}-\bar{r}'\right|}}{4\pi\left|\bar{r}-\bar{r}'\right|} \tag{10}$$

$$\nabla g_i\left(\bar{r},\bar{r}'\right)=\frac{\left(-1+ik_i\left|\bar{r}-\bar{r}'\right|\right)\exp\left(ik_i\left|\bar{r}-\bar{r}'\right|\right)}{4\pi\left|\bar{r}-\bar{r}'\right|}\left(\bar{r}-\bar{r}'\right) \tag{11}$$

In the equations above, k and $g\left(\bar{r},\bar{r}'\right)$ are the wavenumber and Green's function in air, respectively, while k_1 and $g_1\left(\bar{r},\bar{r}'\right)$ are the wavenumber and Green's function for ocean permittivity. Next we apply the MoM to the above surface integral equations. RWG basis functions are used. Curl-conforming RWG functions are used as testing functions. A property of the discretized equations is that the impedance matrix elements are symmetric, e.g.

$$Z_{mn}=Z_{nm} \tag{12}$$

We have used this property to reduce CPU memory and computation time.

A finite surface area of *L* by *L* is used in the surface integral equations. To eliminate the edge effects for a surface with finite size, a tapered plane wave [29], in the form of 2D Fourier transforms, is used:

$$\bar{E}^{inc}\left(\bar{r}\right)=\int_{-\infty}^{\infty}d\bar{k}_\rho e^{i\left(\bar{k}_\rho\cdot\bar{\rho}-k_z z\right)}\psi\left(\bar{k}_\rho\right)\bar{e}\left(\bar{k}_\rho\right) \tag{13}$$

$$\bar{H}^{inc}\left(\bar{r}\right)=\int_{-\infty}^{\infty}d\bar{k}_\rho e^{i\left(\bar{k}_\rho\cdot\bar{\rho}-k_z z\right)}\frac{\psi\left(\bar{k}_\rho\right)}{\eta}\bar{h}\left(\bar{k}_\rho\right) \tag{14}$$

where

$$\bar{r}=\bar{\rho}+\hat{z}z \tag{15}$$

$$\bar{k}_\rho = \hat{x}k_x + \hat{y}k_y \tag{16}$$

and

$$k_z = k_z\left(k_\rho\right) = \begin{cases} \sqrt{k^2 - k_\rho^2}, & 0 \le k_\rho \le k \\ -i\sqrt{k_\rho^2 - k^2}, & k_\rho > k \end{cases} \tag{17}$$

$$\bar{e}\left(\bar{k}_\rho\right) = \bar{e}_i \cdot \left[\hat{h}\left(\bar{k}_\rho\right)\hat{h}\left(\bar{k}_\rho\right) + \hat{v}\left(\bar{k}_\rho\right)\hat{v}\left(\bar{k}_\rho\right)\right] \tag{18}$$

$$\bar{h}\left(\bar{k}_\rho\right) = \bar{e}_i \cdot \left[\hat{v}\left(\bar{k}_\rho\right)\hat{h}\left(\bar{k}_\rho\right) - \hat{h}\left(\bar{k}_\rho\right)\hat{v}\left(\bar{k}_\rho\right)\right] \tag{19}$$

where

$$\bar{e}_i = \bar{e}\left(\bar{k}_{i\rho}\right) = E_h\hat{h}\left(\bar{k}_{i\rho}\right) + E_v\hat{v}\left(\bar{k}_{i\rho}\right) \tag{20}$$

The notations

$$\hat{h}\left(\bar{k}_\rho\right) = \begin{cases} \hat{x}\sin\phi_i - \hat{y}\cos\phi_i, & k_\rho = 0 \\ \dfrac{1}{k_\rho}\left(\hat{x}k_y - \hat{y}k_x\right), & k_\rho > 0 \end{cases} \tag{21}$$

$$\hat{v}\left(\bar{k}_\rho\right) = \begin{cases} \hat{x}\cos\phi_i + \hat{y}\sin\phi_i, & k_\rho = 0 \\ \dfrac{k_z}{kk_\rho}\left(\hat{x}k_x + \hat{y}k_y\right) + \hat{z}\dfrac{k_\rho}{k}, & k_\rho > 0 \end{cases} \tag{22}$$

For fast matrix vector multiplication in the iterative solution of the matrix equation, we used the SMCG method. In the SMCG a Taylor series expansion of Green's function is applied [16] about a flat surface defined by the *x*-*y* plane. Subsequently a 2D FFT is applied. The Taylor series expansions are performed for the Green's functions and the gradient of the Green's functions,

$$g_i(\bar{r},\bar{r}') = \frac{e^{ik_i|\bar{r}-\bar{r}'|}}{4\pi|\bar{r}-\bar{r}'|} = \sum_{m=0}^{M} a_m^{(1,2)}(\rho_R)\left(\frac{z_d^2}{\rho_R^2}\right)^2 \tag{23}$$

$$\nabla g_i(\bar{r},\bar{r}') = \frac{\left(-1+ik_i|\bar{r}-\bar{r}'|\right)\exp\left(ik_i|\bar{r}-\bar{r}'|\right)}{4\pi|\bar{r}-\bar{r}'|}(\bar{r}-\bar{r}') = \sum_{m=0}^{M} b_m^{(1,2)}(\rho_R)\left(\frac{z_d^2}{\rho_R^2}\right)^2 \tag{24}$$

where $z_d = f(x,y) - f(x',y')$. The coefficients above, $a_m^{(1,2)}(\rho_R)$ and $b_m^{(1,2)}(\rho_R)$, are translationally invariant in the horizontal directions. We apply 2D FFTs to the coefficients and these are performed for the product of the Toeplitz matrix and column vector [16]. The first four coefficients of the above expansions, a_m and b_m, are listed in Appendix A. In Appendix A, we also describe improvements to use of SMCG on NMM3D compared with that used in previous implementations.

In this study, the Taylor series are expanded to fifth order. We have checked that 5 terms in Taylor series expansion could give accurate results compared to direct green's function multiplication such that the error norm is less than 0.2% for wind speed 5 m/s. The details of numerical implementation of SMCG on RWG basis functions are also described in appendix A.

2.4 Ocean surface profile generations and L-band backscattering variations with k_l and k_u

For L-band NMM3D simulations, we account for roughness due to both short gravity waves (5 m and less) [32] and shorter gravity-capillary waves (down to 2 cm or so) [33]. Since the wavelength of wind-generated gravity waves will increase with wind forcing, a larger sea surface for the NMM3D analysis is necessary for greater wind speeds. To account for the influence of fine capillary waves on backscatter, a small discretization of the surface is necessary. By varying surface length and discretizations as shown in Table I, we examine the effects of longer gravity

waves and shorter gravity-capillary waves on backscattering at L band. At wind speed 5 m/s, Aquarius data show the Negative Upwind-Crosswind (NUC) asymmetry [33, 37]. This means upwind backscatter is smaller than crosswind backscatter. At other wind speeds (>=8m/s), upwind backscatter are stronger than crosswind. This asymmetry cannot be reproduced based on the DV anisotropic spectrum or using other existing spectrum. We will investigate the spreading function in the future. In the meantime, we use the isotropic DV spectrum for NMM3D for 5 m/s, but upwind data for Aquarius. For 8m/s, the Aquarius data is weakly dependent on wind direction, especially for beam 1 and beam 2. Then we used isotropic surfaces for 8m/s. For 10m/s, we used anisotropic surfaces. We have also calculated surface sample statistics from randomly generated surface profiles [34-36]. The rms heights are provided in Table II for various surface lengths and wind speeds. We have made comparisons between numerical computation and analytical integration and found the ocean statistics within the same spectrum range are the same between the two methods.

Table II Rms for isotropic DV spectrum at different wind speed in terms of longest surface wavelength

Ocean wind speed (m/s)	Surface Length $\boldsymbol{L}(\lambda)$	$\boldsymbol{k_l}$ $(\boldsymbol{m^{-1}})$	rms in centimeters
5	16	1.65	4.8
5	32	0.82	5.5
5	64	0.41	5.5
8	16	1.65	5.1
8	32	0.82	10

8	64	0.41	13.8

For wind speed of 8 m/sec, the increase of surface length from 16 wavelength to 64 wavelength, corresponding to the decrease of k_l, results in an increase of rms height from 5.1 cm to 13.8 cm. This indicates inclusion of longer surface waves with increased surface size.

In order to study the influence of the upper and lower limit of the spectral range used in the simulation, we conducted NMM3D simulations using different surface lengths and discretizations.

Table III VV and HH for varying discretizing densities at wind = 5 m/s with 39° incidence angle and isotropic DV spectrum compared with upwind Aquarius data

$\Delta x, \Delta y$ (λ)	$k_u(m^{-1})$	VV(dB)	HH(dB)	# of realizations
1/16	211	-15.42	-20.45	30
1/32	211	-15.49	-20.27	30
Aquarius	N/A	-15.50	-20.00	N/A

Table III shows the backscatter results for wind speed = 5 m/s at several sampling densities. The results show that 16 points per wavelength and 32 points per wavelength yield very similar backscattering results. The difference is within 0.3 dB. The Aquarius upwind data are also listed in the table. Based on extensive simulations, sampling at 16 points per wavelength yields sufficient accuracy to account for the small scale roughness. Including smaller capillary wave roughness does not alter the backscattering results for this case. For emissivity calculations, denser sampling

are required. And results for cross wind and upwind are compared for the anisotropic DV spectrum and are shown in Figure 5.

Next we conducted numerical simulations for several surfaces sizes at winds of 5 and 8 m/s. These correspond to changing k_l. The backscatter results are shown in Table III. We also include in Table III and IV the number of realizations used in the simulations as shown in the last column of the two tables. We have conducted convergence test with the number of realizations. Results show that 30 realizations can give stable results for backscatter. For the 16λ case, the computation time is about 3~4 minutes for each realization. For the 32 λ case, it is about 20 minutes for each realization. For the 64λ case, it is about 1 hour for each realization. The convergence rate of iterations is influenced by the roughness of the ocean surface.

Table IV VV and HH for L band 39° incidence isotropic DV spectrum compared with Upwind Aquarius data

(a)

VV and HH for varying surface sizes at wind=5 m/s

Surface Size	$\boldsymbol{k_l}$ $(\boldsymbol{m^{-1}})$	VV(dB)	HH(dB)	# of realizations
$16 \times 16\lambda^2$	1.65	-15.42	-20.45	30
$32 \times 32\lambda^2$	0.82	-15.54	-20.71	30
$64 \times 64\lambda^2$	0.41	-15.50	-20.50	30
Aquarius	N/A	-15.50	-20.00	N/A

(b)

VV and HH for varying surface sizes at wind= 8 m/s

Surface Size	$\boldsymbol{k_l}$ $(\boldsymbol{m^{-1}})$	VV(dB)	HH(dB)	# of realizations

$16 \times 16\lambda^2$	1.65	-14.72	-19.75	30
$32 \times 32\lambda^2$	0.82	-14.65	-19.51	30
$64 \times 64\lambda^2$	0.41	-14.06	-19.34	29
Aquarius	N/A	-14.80	-18.65	N/A

The NMM3D backscatters of various simulated surface sizes are shown in Table IV (a) and (b) for wind 5 m/s and 8 m/s, respectively. It is noted that there is a less than 1dB difference for VV, a 1.4 dB difference for HH at 5 m/s and 8 m/s. One observes that for the two wind speeds, the maximum difference for backscatter for varying surface sizes is 0.7 dB. There is also an increase of backscatter with increasing wind speed from table (a) to table (b). It is to be noted that from table (c), the 3 surface sizes at wind 8 m/s have approximately the same backscatter. But in Table II, the 3 surface sizes have very different rms height for the same wind speed of 8m/sec. With the increase of simulated surface size, longer waves (waves that are meters long and have a large rms height) are included in the simulations. However, these longer waves do not cause significant differences on backscatter at 8 m/s. The backscatter arises from the spectral components in the ocean spectrum that are comparable to the wavelength of the incoming microwaves. For L band, the decimeter and centimeters ocean waves cause backscatter. The above convergence analysis may also be influenced by the random errors brought by the Monte Carlo simulations. In future studies, the use of larger surface sizes will be studied.

2.5 NMM3D results and discussions

In this section, we present NMM3D numerical ocean scattering results at L-band and their comparison with Aquarius data. The assumed surface relative permittivity is 75+61i, corresponding to a complex index of refraction of 9.26+3.29i. This is the case of seawater with a salinity of 35 ppt (parts per thousand) at water temperature of 10^{o}C at 1.26 GHz. For each

realization, a single sea surface is generated and Maxwell's equations are solved numerically. The scattering coefficients represent results averaged over 30~300 realizations.

Isotropic and anisotropic Durden-Vesecky ocean spectrum are used for simulations of wind-dependent L-band backscatter. The isotropic DV spectrum is used for 5 m/sec and 8 m/sec. The anisotropic DV spectrum is used for 10m/sec [38, 40].

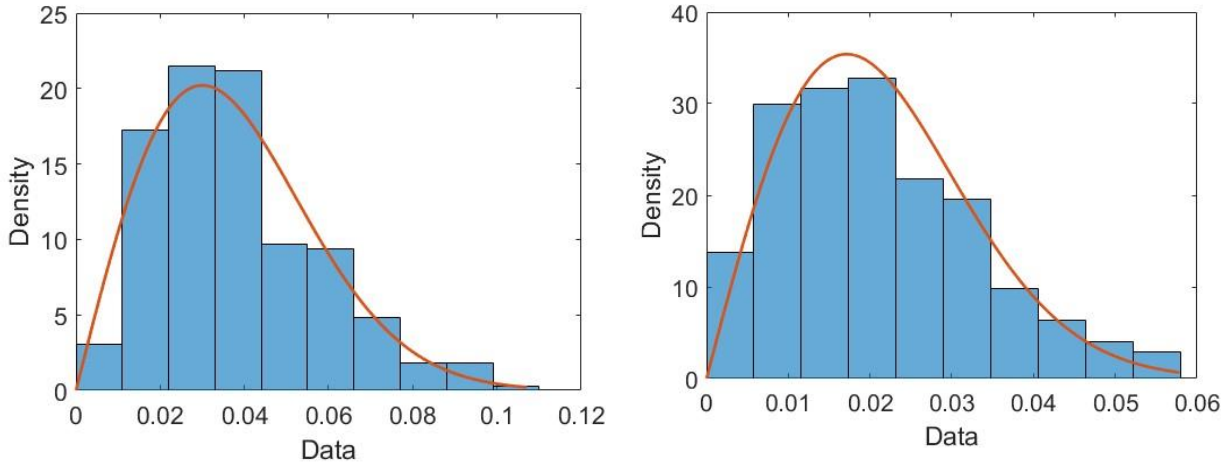

Figure 2 Comparison of L-band NMM3D scattering amplitude distributions for 300 realizations for co-polarized cases VV (left), HH(right) and for wind speed of 5 m/s using the isotropic DV spectrum and an incidence angle 29^{o}. The red curve indicates that for a Rayleigh-distributed process.

Figure 2 shows the statistical distributions of the simulated results for HH, VV computed using 300 realizations with a wind of 5 m/s and incidence angle of 29^{o}. The histogram of computed backscatter values is consistent with that shown for a Rayleigh distribution.

Figure 3 shows the in-plane bistatic L-band scattering coefficients at 5 m/s wind speed and 39 degree incidence. In these simulations we decompose the bistatic scattering coefficients into coherent and incoherent waves [13, 15]. For the surface sizes used, the coherent waves are only significant in the specular direction while scattering in other directions arises from the incoherent waves [13-15, 39, 40]. The backscattering direction is highlighted with a dashed line in Figure 3.

Figure 4 shows the backscatter dependence at the three incidence angles of the Aquarius scatterometer, 29°, 39°, 46° at wind = 5 m/s. Backscattering decreases with incidence angle. The upwind Aquarius data are also shown. For co-polarization, the agreement between simulations and upwind Aquarius data are within 1 dB at the three incidence angles.

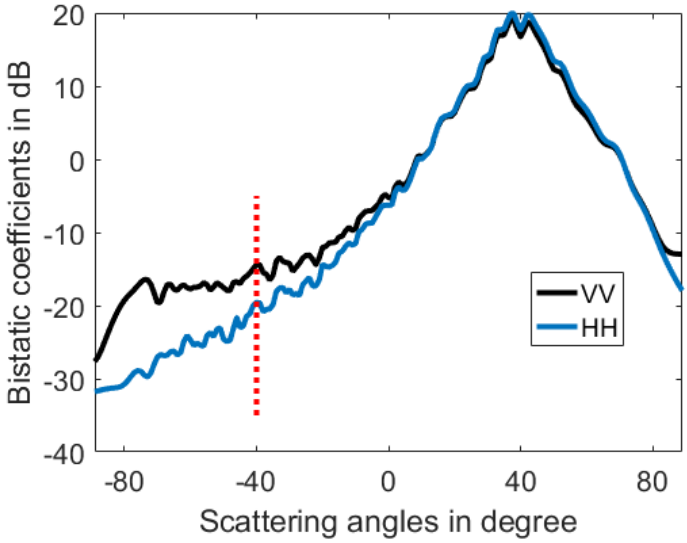

Figure 3 In-plane bistatic VV HH for wind = 5m/s isotropic DV spectrum

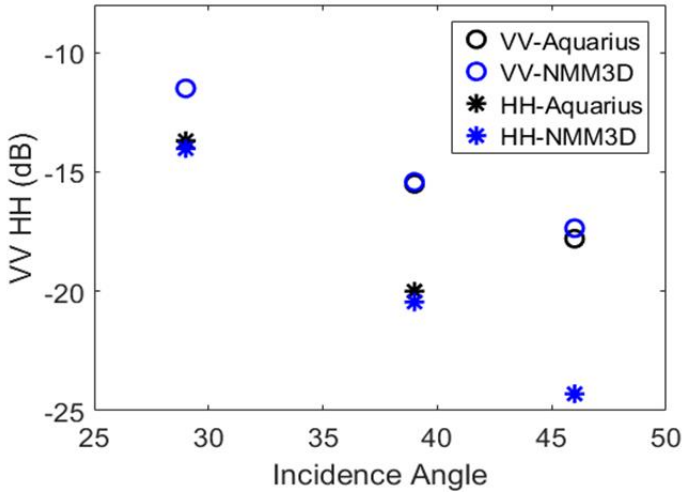

Figure 4 L-band backscatter at wind speed = 5 m/s for different incidence angles: 29, 39, 46 degrees and isotropic DV spectrum compared with upwind Aquarius data.

In Figure 5, we illustrate the backscatter for wind = 10 m/s using an anisotropic DV spectrum. The incidence angle is 46°. There are 4 curves in the figures: NMM3D with error bars derived from the Monte Carlo simulations, first order SPM, Aquarius data, and composite surface model (two scale model). There are several TSM models because TSM is a heuristic approximation, subdividing the objects into parts and them performing incoherent combining with tilts. We have referred to several TSM models in our computation. The uncertainty of numerical simulation is defined as

$$error\ (dB) = 10\log 10(1+\frac{1}{\sqrt{N}}) \tag{25}$$

for VV, HH. In (25), N is the number of realizations. The 4 panels in Figure 4 correspond to VV, HH, VV/HH (polarization ratio), VH, respectively. We can see that HH of SPM is lower than Aquarius data, while NMM3D, TSM, and SPM show VV results that are all comparable with Aquarius observations. The polarization ratio, VV/HH, derived using SPM is 1.5dB larger than the data. NMM3D and TSM can both give good polarization ratio compared to data while polarization ratio given by SPM is larger than data and not changing with data. For current wind speeds (wind speed<10m/s) we are studying, TSM and NMM3D both agree well with data for cross polarization. The figure also indicates that Aquarius data show a directional dependence in the polarization ratio. A wind direction dependence for this ratio is also exhibited in NMM3D, while the ratio is direction-invariant for SPM. With a diving wavenumber equals $\frac{k_0}{2}$, we see that TSM can predict good scattering coefficient as NMM3D.

Figure 6 provides the backscattering polarization ratio for winds of 8 and 10m/s and for the three incidence Aquarius angles [40]. NMM3D simulation uncertainties are also shown. For

wind=8m/s, the surfaces used in the computations are derived from the isotropic DV spectrum. The results of TSM and data shown in Figure 6 are averaged over all wind directions. For wind=10m/s, the anisotropic DV spectrum is used in NMM3D. The results of NMM3D, TSM and Aquarius data are also averaged over all wind directions. Results indicate that the VV/HH ratio increases with increasing incidence angle. From the figures, we see that the difference for both TSM and NMM3D compared to Aquarius data are both within 0.6dB.

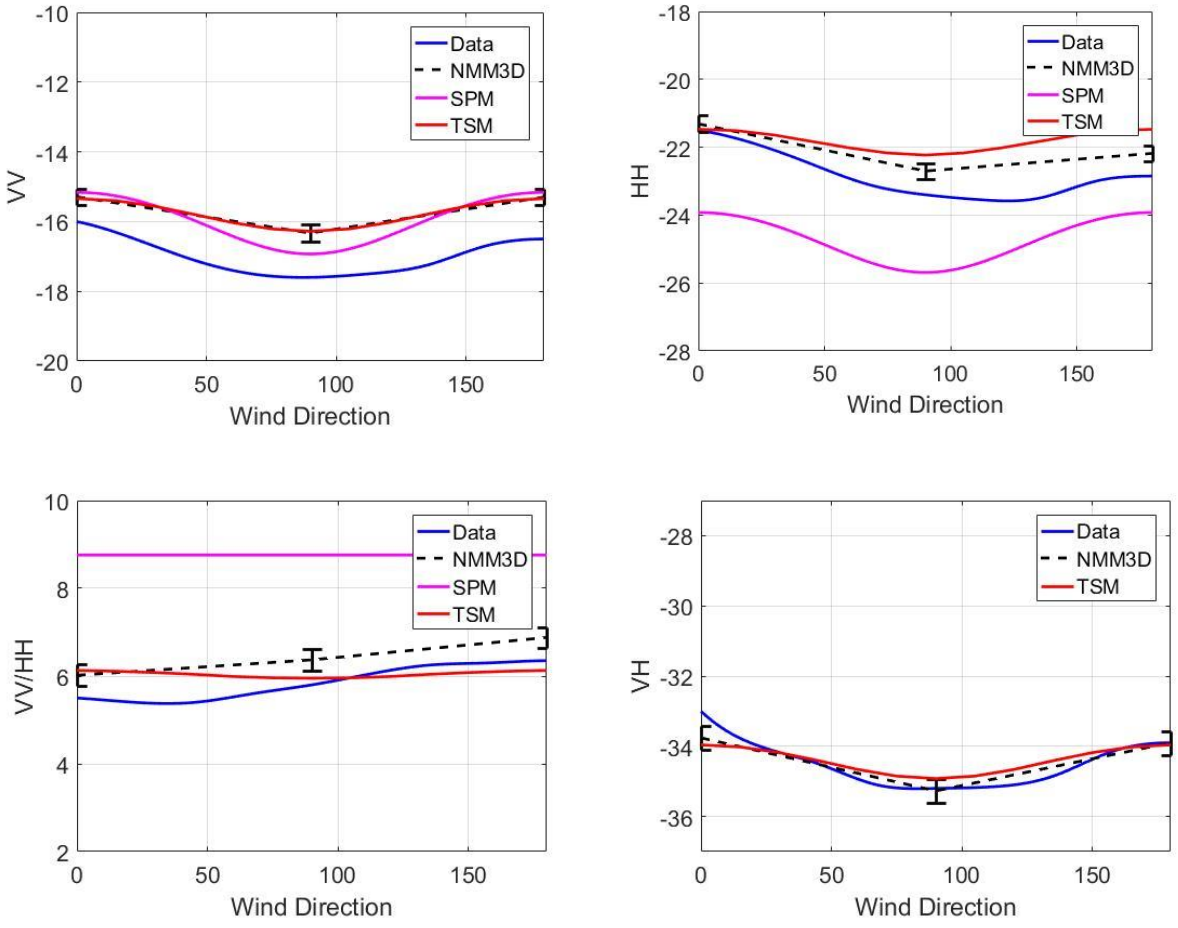

Figure 5 L-band backscatter for wind speed =10 m/s and incidence angle= 46°. Upper two panels are VV and HH, and bottom is for VV/HH. TSM, NMM3D, SPM results use the anisotropic DV spectrum.

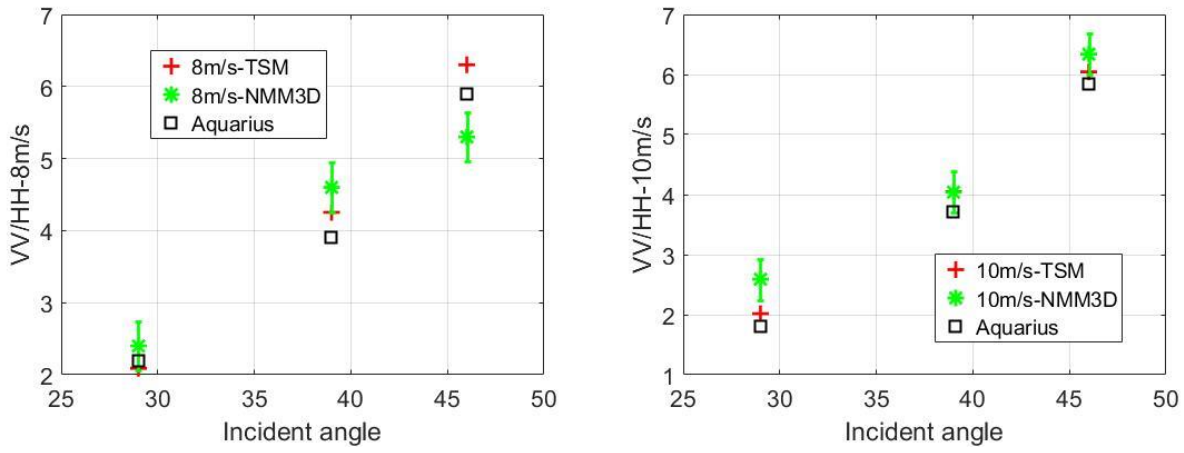

Figure 6 Comparison of NMM3D and two scale model of VV/HH with Aquarius at 29º, 39º, and 46º. NMM3D is using isotropic DV spectrum for 8 m/s and anisotropic DV spectrum for 10 m/s. TSM is derived using the anisotropic DV spectrum for wind = 8 and 10m/s. Each data point is obtained by averaging over all wind directions.

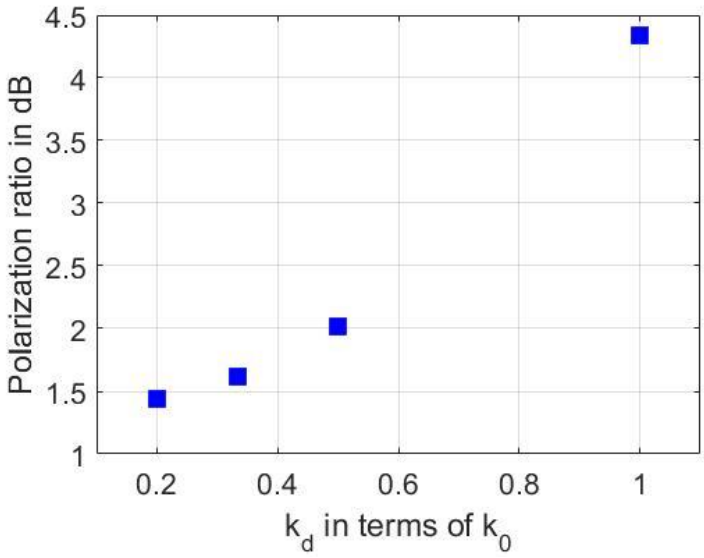

Figure 7 Polarization ratio for wind speed 10m/s and 26° incidence. The horizontal axis is different cutoff wavenumbers. Vertical axis is VV/HH ratio in dB. Each data point is obtained by averaging over all wind directions.

In Figure 7 we plotted the polarization ratio for wind speed 10m/s and 26° incidence. The horizontal axis is different cutoff wavenumbers. Vertical axis is VV/HH ratio in dB. Each data point is obtained by averaging over all wind directions. It is apparent that the polarization ratio is changing with different cutoff wavenumbers. And for such a case, we see that $k_d = k_0$ will result in a VV/HH ratio 3dB higher than $k_d = \frac{k_0}{5}$.

2.6 Conclusions

With an efficient SMCG method implemented to solve the PMCHWT surface integral equations, we have performed NMM3D simulations for ocean radar scattering at L band frequencies. Surface areas used are up to 15.2 m by 15.2 m (64 wavelengths). For the largest surfaces, there are more than 6 million surface unknowns in the tangential electric and magnetic fields. This use of a large surface for simulations allows us to examine the effects of gravity and capillary waves. The numerical simulations, unlike the two-scale scattering model, does not require a wavenumber dividing line between large and small scale roughness. Simulations are shown for 5m/sec, 8m/sec and 10m/sec using isotropic DV spectrum and anisotropic DV spectrum. The backscatter results are in good agreement with Aquarius observation data for VV and HH co-polarization, cross-polarization, and VV/HH ratio. A rigorous approach to the problem based on NMM3D is to incrementally increase the surface size until convergence is reached. Recent computational electromagnetic efforts about scattering by large objects are on using rigorous domain decomposition which should be considered in remote sensing simulations. Without a large domain, it is possible that tilt effects are not included. To obtain tilt effects require a definition of decomposition and tilts can both decrease or increase local incident angles, requiring a heuristic use of tuning parameters. For inclusion of tilt effects, the readers can refer to reference [7]. For NMM3D to move forward, the increase of domain size via domain decomposition and the increase

of sampling points per wavelength are essential steps. Also, the authors has used $\frac{k_0}{2}$ as the dividing wavenumber in the TSM for separation of applying SPM and Geometrical Optics. The results produced by TSM match well with Aquarius. But if using other dividing wavenumbers, the scattering coefficients are not good. This indicate TSM is quite an ad hoc method.

Appendix A

In order to integrate SMCG with the PMCHWT equation, it is necessary to write the equation in a form where the field and source points are separated. We will use the subscript *m* to denote the field point and subscript *n* to denote the source point. The superscripts *x*, *y*, and *z* represent the three axes. The following discretized impedance matrix expressions are obtained after performing moment method operations to the kernel of the electric field integral equation (EFIE)

$$\int_{S_m}\int_{S_n}\left(\bar{f}_m\cdot\bar{f}_n-\frac{1}{k^2}\nabla\cdot\bar{f}_m\nabla'\cdot\bar{f}_n\right)g\left(\bar{r},\bar{r}'\right)d\bar{r}d\bar{r}' \tag{26}$$

where $\bar{f}_m$ and $\bar{f}_n$ are the RWG basis functions for the field and source edges. Also

$$\begin{aligned}\bar{f}_m\left(\bar{r}\right)g\left(\bar{r},\bar{r}'\right)\cdot\bar{f}_n\left(\bar{r}'\right)=&\ f_m^x\left(\bar{r}\right)g\left(\bar{r},\bar{r}'\right)f_n^x\left(\bar{r}'\right)\\&+f_m^y\left(\bar{r}\right)g\left(\bar{r},\bar{r}'\right)f_n^y\left(\bar{r}'\right)\\&+f_m^z\left(\bar{r}\right)g\left(\bar{r},\bar{r}'\right)f_n^z\left(\bar{r}'\right)\end{aligned} \tag{27}$$

$$\nabla\cdot\bar{f}_m g\left(\bar{r},\bar{r}'\right)\nabla'\cdot\bar{f}_n=\left(\pm\frac{l_m}{S_m^{\pm}}\right)g\left(\bar{r},\bar{r}'\right)\left(\pm\frac{l_n}{S_n^{\pm}}\right) \tag{28}$$

The kernel of the magnetic field integral equation (MFIE) is:

$$\begin{aligned}&\bar{f}_m\left(\bar{r}\right)\times\nabla g\left(\bar{r},\bar{r}'\right)\cdot\bar{f}_n\left(\bar{r}'\right)\\&=\bar{f}_m\left(\bar{r}\right)\times\frac{\left(-1+ik\left|\bar{r}-\bar{r}'\right|\right)\exp\left(ik\left|\bar{r}-\bar{r}'\right|\right)}{4\pi\left|\bar{r}-\bar{r}'\right|}\left(\bar{r}-\bar{r}'\right)\cdot\bar{f}_n\left(\bar{r}'\right)\end{aligned} \tag{29}$$

We use

$$G\left(\bar{r},\bar{r}'\right)=\frac{\left(-1+ik\left|\bar{r}-\bar{r}'\right|\right)\exp\left(ik\left|\bar{r}-\bar{r}'\right|\right)}{4\pi\left|\bar{r}-\bar{r}'\right|} \tag{30}$$

Then

$$
\begin{aligned}
&\bar{f}_m(\bar{r})\times\nabla g(\bar{r},\bar{r}')\cdot\bar{f}_n(\bar{r}') \\
&=\bar{f}_m(\bar{r})\times(\bar{r}-\bar{r}')\cdot\bar{f}_n(\bar{r}')G(\bar{r},\bar{r}') \\
&=f_m^{\,y}r_m^{x}G(\bar{r},\bar{r}')f_n^{\,z}-f_m^{\,z}r_m^{x}G(\bar{r},\bar{r}')f_n^{\,y}-f_m^{\,y}G(\bar{r},\bar{r}')f_n^{\,z}r_n^{x}+f_m^{\,z}G(\bar{r},\bar{r}')f_n^{\,y}r_n^{x} \\
&+f_m^{\,z}r_m^{y}G(\bar{r},\bar{r}')f_n^{\,x}-f_m^{\,x}r_m^{y}G(\bar{r},\bar{r}')f_n^{\,z}-f_m^{\,z}G(\bar{r},\bar{r}')f_n^{\,x}r_n^{y}+f_m^{\,x}G(\bar{r},\bar{r}')f_n^{\,z}r_n^{y} \\
&+f_m^{\,x}r_m^{z}G(\bar{r},\bar{r}')f_n^{\,y}-f_m^{\,y}r_m^{z}G(\bar{r},\bar{r}')f_n^{\,x}-f_m^{\,x}G(\bar{r},\bar{r}')f_n^{\,y}r_n^{z}+f_m^{\,y}G(\bar{r},\bar{r}')f_n^{\,x}r_n^{z}
\end{aligned}
\tag{31}
$$

Equation (27) (28) and (31) are in a form such that the source point is on the right side of Green's function while the field point resides on the left side of Green's function. Next the Green's function is expanded in a Taylor series with respect to the flat surface. The first 4 coefficients are listed in equations (32) to (39).

$$
a_0^{(1,2)}(\rho_R)=\left(1-ik_{1,2}\rho_R\right)\frac{\exp\left(ik_{1,2}\rho_R\right)}{4\pi\rho_R} \tag{32}
$$

$$
a_1^{(1,2)}(\rho_R)=\frac{\exp\left(ik_{1,2}\rho_R\right)}{4\pi\rho_R}\left\{\frac{k_{1,2}^2}{2\rho_R}+\frac{3ik_{1,2}}{2\rho_R^2}-\frac{3}{2\rho_R^3}\right\} \tag{33}
$$

$$
a_2^{(1,2)}(\rho_R)=\frac{\exp\left(ik_{1,2}\rho_R\right)}{4\pi\rho_R}\left\{\frac{ik_{1,2}^3}{8}-\frac{6k_{1,2}^2}{8\rho_R}-\frac{15ik_{1,2}}{8\rho_R^2}+\frac{15}{8\rho_R^3}\right\} \tag{34}
$$

$$
a_3^{(1,2)}(\rho_R)=\frac{\exp\left(ik_{1,2}\rho_R\right)}{4\pi\rho_R}\left\{-\frac{k_{1,2}^4\rho_R}{48}-\frac{10ik_{1,2}^3}{48}+\frac{105k_{1,2}^2}{112\rho_R}+\frac{35ik_{1,2}}{16\rho_R^2}-\frac{35}{16\rho_R^3}\right\} \tag{35}
$$

$$
b_0^{(1,2)}(\rho_R)=\frac{\exp\left(ik_{1,2}\rho_R\right)}{4\pi\rho_R} \tag{36}
$$

$$
b_1^{(1,2)}(\rho_R)=\exp\left(ik_{1,2}\rho_R\right)\left\{\frac{ik_{1,2}}{8\pi}-\frac{1}{8\pi\rho_R}\right\} \tag{37}
$$

$$
b_2^{(1,2)}(\rho_R)=\exp\left(ik_{1,2}\rho_R\right)\left\{-\frac{k_{1,2}^2\rho_R}{32\pi}-\frac{3ik_{1,2}}{32\pi}+\frac{3}{32\pi\rho_R}\right\} \tag{38}
$$

$$b_3^{(1,2)}(\rho_R)=\exp(ik_{1,2}\rho_R)\left\{-i\frac{k_{1,2}^3\rho_R^2}{192\pi}+\frac{k_{1,2}^2\rho_R}{32\pi}+\frac{13ik_{1,2}}{192\pi}-\frac{13}{192\pi\rho_R}\right\} \tag{39}$$

We have used the centroid as the integration point within each triangular patch [26].

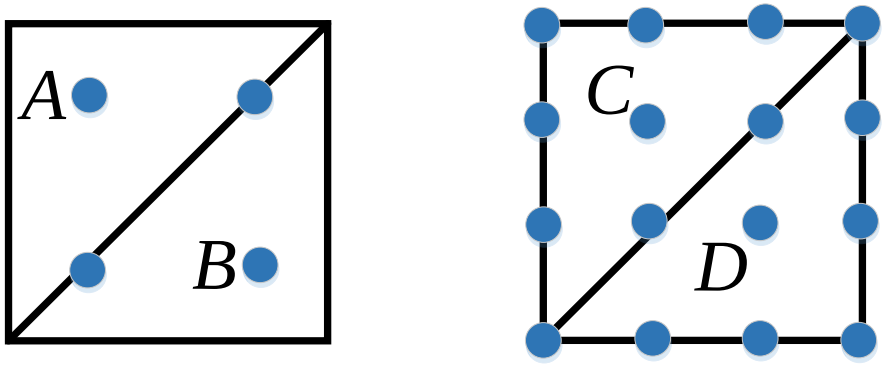

(a) (b)

Figure 8 SMCG with centroid as integration points

As is shown in Figure 8 (a), the local coordinates of the two integration points *A* and *B* are (1/4, 3/4) and (3/4, 1/4) which are not centroids of the two triangles. In Figure 8 (b), the local coordinates of *C* and *D* are (1/3, 2/3) and (2/3, 1/3), respectively. The points *C* and *D* fall onto the center of each triangle. After making the modification from (a) to (b), the accuracy of SMCG is greatly improved.

We define the error of SMCG by

$$error=\frac{\left\|z_{mn}-z_{mn}^{SMCG}\right\|}{\left\|z_{mn}\right\|} \tag{40}$$

where z_{mn} are the impedance matrix elements calculated directly using 7th order quadrature and z_{mn}^{SMCG} are the matrix elements calculated indirectly by the SMCG method. For a 4λ by 4λ

surface with 16 points per wavelength, the error is about 0.2%. In addition to SMCG, we have also used Green's function interpolation in the numerical simulations [9].

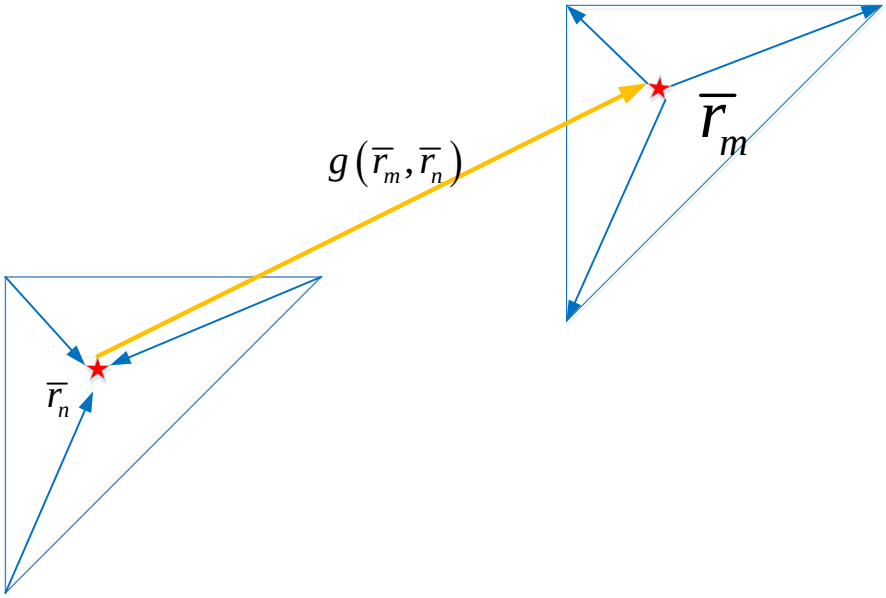

Figure 9 SMCG in conjunction with RWG basis functions

In Figure 9, we illustrate how SMCG based on RWG functions works. Firstly, the currents inside one source triangle patch aggregates to the centroid. Next, the accumulated currents transfer to the field triangle through Green's function. Then the transferred field distributes to each inner edge inside the source triangle.

Appendix B

The ocean surface height spectrum for a fully-developed wind sea, as proposed by Durden and Vesecky [21], has the following form:

$$W_{DV}\left(k.\phi\right)=\frac{a_0}{2\pi k^4}\Phi_{DV}\left(k,\phi\right)\begin{cases}\exp\left(-\dfrac{\beta g^2}{k^2U_{19.5}^4}\right) & k<k_j\\ \left(\dfrac{bku_*^2}{g_*}\right)^{a\log_{10}(k/2)} & k\geq k_j\end{cases} \tag{41}$$

where $k_j=2m^{-1}$. The subscript DV denotes the Durden-Vesecky spectrum. The constant a_0 is 0.004 in [21], but was adjusted upwards to 0.008 in Yueh et al. [20]. In order to best fit the L-band measurement data in this study, a value of $a_0=0.008\cdot1.3$ is applied. Other parameters are $\beta=0.74$, $b=1.25$, $a=0.225$, $g_*=g+\gamma k^2$, $g=9.81m/\sec^2$ is acceleration due to gravity, and $\gamma=7.25\times10^{-5}m^3/\sec^2$ is the ratio of surface tension to water density. The wind friction velocity at the ocean surface, u_*, is related to the wind speed at a height (h) of 19.5 meter above sea level, $U_{19.5}$, using the following form.

$$U_h=\frac{u_*}{0.4}\log\frac{h}{0.0000684/u_*+0.00428u_*^2-0.000443} \tag{42}$$

The wave directional spreading factor $\Phi\left(k,\phi\right)$ is

$$\Phi(k,\phi)=1+\Delta(k)(1-\exp(-sk^2))\cos(2(\phi-\phi_{wind})) \tag{43}$$

In (43), the upwind direction is defined as $\phi_{wind}=0^o$. In this chapter, $\Delta\left(k\right)$ is defined as

$$\Delta\left(k\right)=c\frac{\left(1-R\right)}{\left(1+R\right)}\frac{2}{1-D} \tag{44}$$

with

$$R = \frac{0.003 + 1.92 \times 10^{-3} U_{12.5}}{3.16x10^{-3} U_{12.5}} \tag{45}$$

$$D = \frac{\int_0^\infty dkk^2 S(k) \exp\left(-sk^2\right)}{\int_0^\infty dkk^2 S(k)} \tag{46}$$

Chapter 3 Radar Scattering of Ocean Surfaces with Anisotropic Ocean Spectrum using NMM3D simulations

3.1 Introduction

Recent years have seen an increase in L-band microwave satellite sensors in earth remote sensing applications. This wavelength benefits from near atmospheric transparency, the ability to retrieve soil moisture information, sense and penetrate snowpack, and respond to ocean surface wind and salinity [45]. Studies have recently been conducted for ocean backscattering at L band using PALSAR and Aquarius radar data [38].

Because ocean wind create anisotropy in ocean surfaces, the radar cross section have interesting azimuthal directional dependences. There is a new puzzle for L band in directional dependence in all polarizations: the upwind backscatter is larger than the crosswind backscatter for high winds (>10 m/s), but the relative amplitude changes at lower wind speeds (<8 m/s). This is termed a Negative Upwind-Crosswind (NUC) asymmetry.

Figure 10 shows the Geophysical Model Function (GMF) of Aquarius scatterometer for different wind direction. The incidence angle is 29 degree. The figure shows that for wind speeds larger than 8 m/s, backscatter of crosswind is smaller than that of upwind. But for wind speeds of 5 m/s and 8 m/s, the backscatter at crosswind is larger than that of upwind. This phenomenon is also shown in PALSAR [35] which is L band. However it not observed in higher frequency bands.

Analytical models, AIEM or TSM, using common adopted ocean spectrum, cannot reproduce the NUC phenomenon. Yueh et al. (2013) suggested that directional and passive/active aspects of the signals might correspond to a non-Bragg scattering phenomena at L-band.

Alternatively, it is possible that the surface waves themselves have markedly different directional distribution near the L-band, ultragravity 20-50 cm wavelengths, at these low to moderate wind speeds.

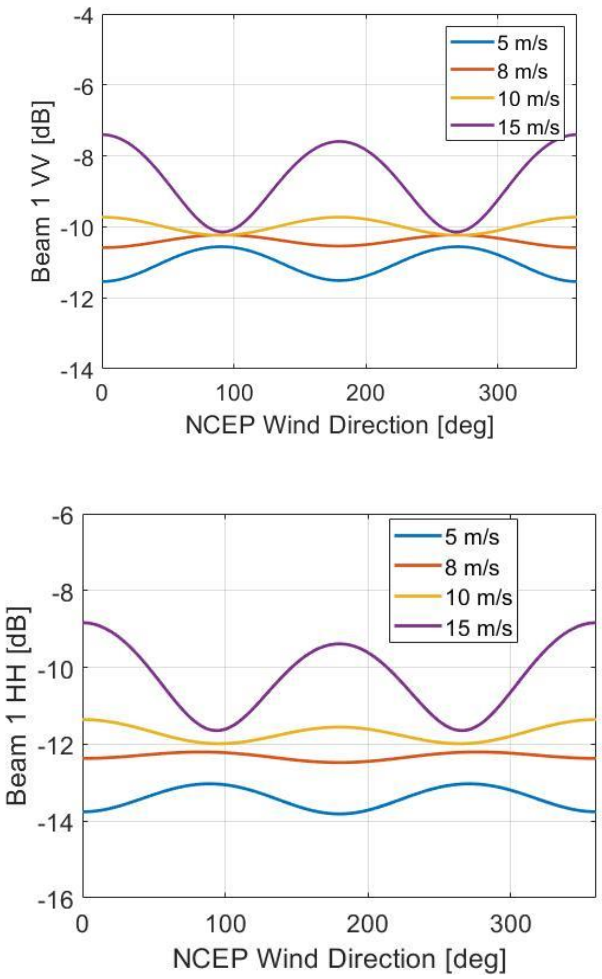

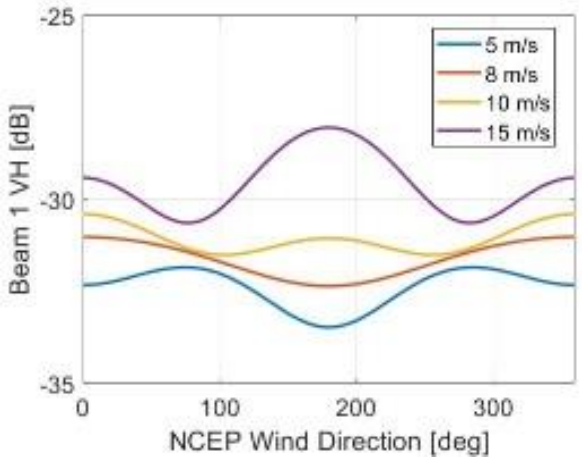

Figure 10 Geophysical Model Function of Aquarius scatterometer data versus wind direction of beam 1 at L band. Top figure is VV, middle figure is HH, bottom figure is VH. The four curves correspond to wind speeds 5, 8, 10, 15 m/s.

In addition to analytical modeling of surface scattering problems, numerical simulations of 3D rough surface scattering have become feasible by combining fast numerical methods and high performance computing. The simulations have been applied to land and ocean surfaces[11, 12, 44, 46]. In [44], it is proved that the NMM3D results could predict the backscatter well compared to Aquarius data and analytical method. On the other, the input for the numerical method is the computer generated ocean surfaces which can include a large range of different ocean wave scales. This is advantageous compared to many analytical methods which only one point on the ocean spectrum is used.

In this chapter, we study the NUC through both analytical method and numerical simulations at L band under 5 m/s. Two kinds of surfaces are studied: Elfouhaily spectrum with/without horseshoe patterns and the Apel spectrum with modified angular spreading function [43]. In the following ocean spectrum is introduced and then results generated from NMM3D are shown and analysis are conducted.

3.2 Ocean spectrum

Ocean spectrum is used to characterize the power distribution of ocean waves on different scales of waves and on different directions. In the past we studied soil surfaces with exponential correlation functions [11, 46].Compared to rough land surface, ocean surface is smoother. This is also illustrated in Figure 11.

Figure 11 shows a comparison of spectrum between ocean (Pierson-Moskowitz), spectrum of Gaussian and exponential correlation function. The three curves have the same rms height which is 0.06 meter. The correlation length is 10 times rms height. It is clear that exponential function has a much higher tail than ocean spectrum. This means soil land surfaces have much finer features than sea surface. Gaussian surface is even smoother.

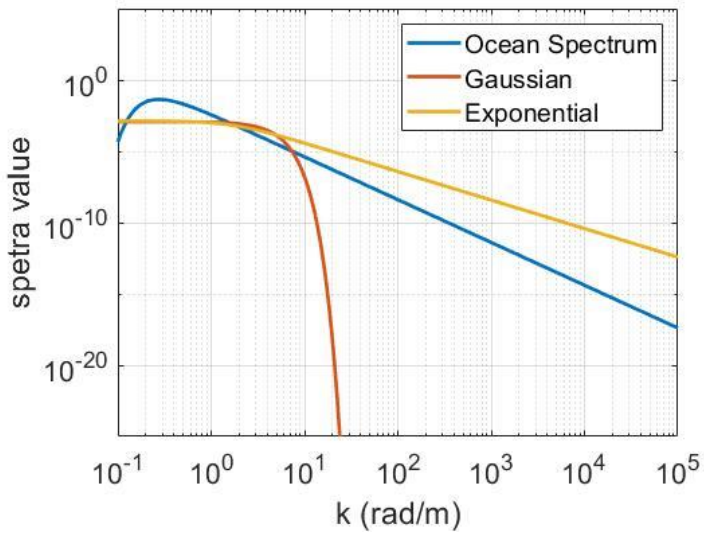

Figure 11 Comparison of Ocean (Pierson-Moskowitz), Gaussian and Exponential Spectrum for the same RMS height. Correlation length for Gaussian and exponential spectrum density is 10 times rms height.

From ocean spectrum, the sea surface profiles are generated using spectrum for varying wind speeds using linear and nonlinear methods. The basic assumption underlying linearity of the surface is that the surface is a linear combination of different scales of sinusoidal waves.

Figure 12 plots the computer generated ocean surface using linear method by Elfouhaily spectrum. The dimension is 15.2m by 15.2m. The wind speed is 5m/s.

In this chapter we simulate L-band backscattering from anisotropic ocean surface with NMM3D. Two kinds of ocean surface profiles are used for NMM3D simulations. One is a group of time series nonlinear profiles generated by combining the nonlinear gravity waves and shorter "horse-shoe" pattern using Elfouhaily spectrum. The other is a group of linear profiles generated from a newly developed directional spectrum [43]. The introductions and analyses of these two kinds of profiles are given in the following sections.

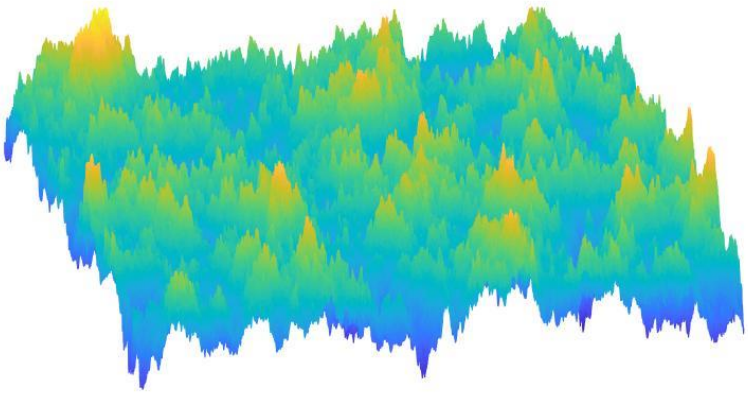

Figure 12 Computer generated linear ocean surface at 5 m/s using Elfouhaily spectrum. The dimension is 15.2m by 15.2m.

3.2.1 Nonlinear ocean surface profiles

In addition to linear ocean surfaces, non-linear ocean surface is more popular due to its matching with ocean hydrodynamics. The profiles we are using is the Choppy Wave Model (CWM) with/without horsehose patterns.

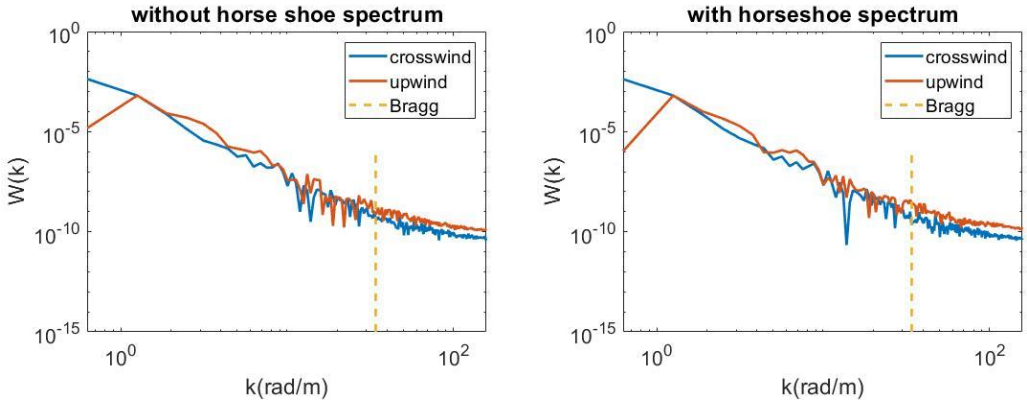

Figure 13 Extracted ocean spectrum for 5m/s with and without horseshose patterns of Choppy Wave Model for upwind and downwind.

Figure 13 shows the extracted ocean spectrum for 5m/s with and without horseshoe patterns of Choppy Wave Model. The ocean spectrum used is anisotropic Elfouhaily spectrum. The profiles are of time series with 0.1 second as the time interval of total 2 seconds. It is seen that for *k* around the Bragg wavenumber, upwind is stronger than crosswind. Generally the upwind is stronger than crosswind for all the wavenumber ranges. The surface length of the profiles are 8 meters.

3.2.2 A newly developed directional wave spectrum

Another surface profiles that have been used is linear ocean surface generated by Apel spectrum using the spreading function by Du et al., 2017 [43]. The angular spreading function is obtained by data fitting between Aquarius measurement and AIEM using Apel spectrum.

Figure 14 illustrates the $\Delta(k)$ function of Du's spectrum for the anisotropic surface for 5 8 and 10 m/s. We could see that different from many other spectrum, the $\Delta(k)$ function is negative for *k* ranges from 10 to around 80 rad/m. If using first order SPM to simulate backscatter, we will

get the backscatter is larger in crosswind than upwind at L band. This is because the input of first order SPM is the Bragg point in the spectrum curve. And we have Bragg wavenumber equal 33 rad/m for 39 incidence and 1.26GHz. Then

$$\left[1+\Delta(33)\cos(0)\right] < \left[1+\Delta(33)\cos(2\cdot\frac{\pi}{2})\right] \tag{47}$$

The new angular spreading function (ASF) is expressed as

$$\Phi(k,\phi) = \left[1+\Delta(k)\cos(2\phi)\right] \tag{48}$$

$$\Delta(k) = \tanh\left[a_0 + a_d \cdot S_d + a_p\left(c/c_p\right)^{2.5} + a_m\left(c_m/c\right)^{2.5}\right] \tag{49}$$

$$S_d = \tanh\left[u^* \cdot k_x + \frac{g}{c_p^2 \cdot k_x} - \frac{20}{c_p}\sqrt{g\cdot u^{*2.55}} + 2.55\cdot u^*\right] \quad k_x = k^{1.1}\cdot c_m^{1.65} \tag{50}$$

$$u^* = u_{10}\cdot\sqrt{0.001\cdot\left(0.81+0.065\cdot u_{10}\right)} \tag{51}$$

$$a_m = 0.26\frac{u^*}{c_m} \tag{52}$$

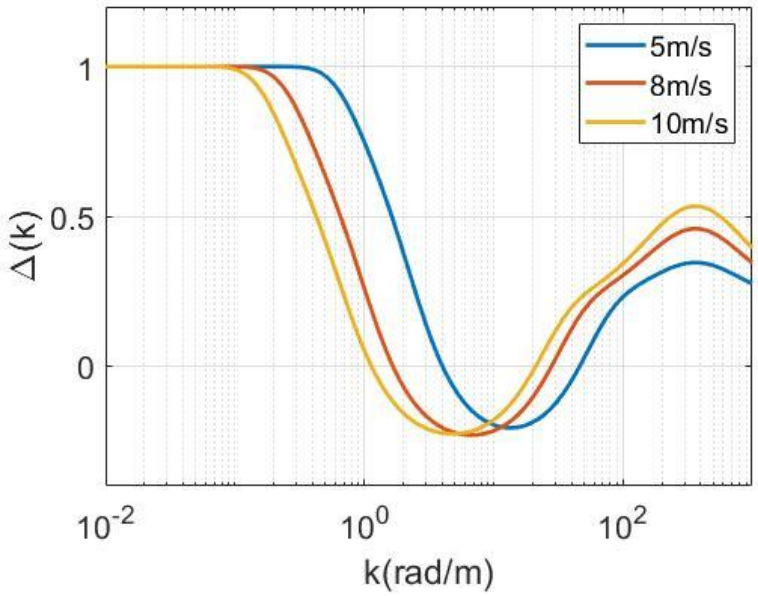

Figure 14 $\Delta(k)$ of Du's spectrum for wind speed 5 8 and 10 m/s.

In equation (49), c is the wave phase speed and c_p is the phase speed of the dominant long wave. The relationship between wave phase speed c and wavenumber k can be written as

$$c = \sqrt{g/k\left[1+\left(\frac{k}{k_m}\right)^2\right]} \tag{53}$$

$$a_0 = -\ln(2)/4 \quad a_d = \ln(2)/2 \quad a_{p=4} \quad c_m = 0.23m/s \tag{54}$$

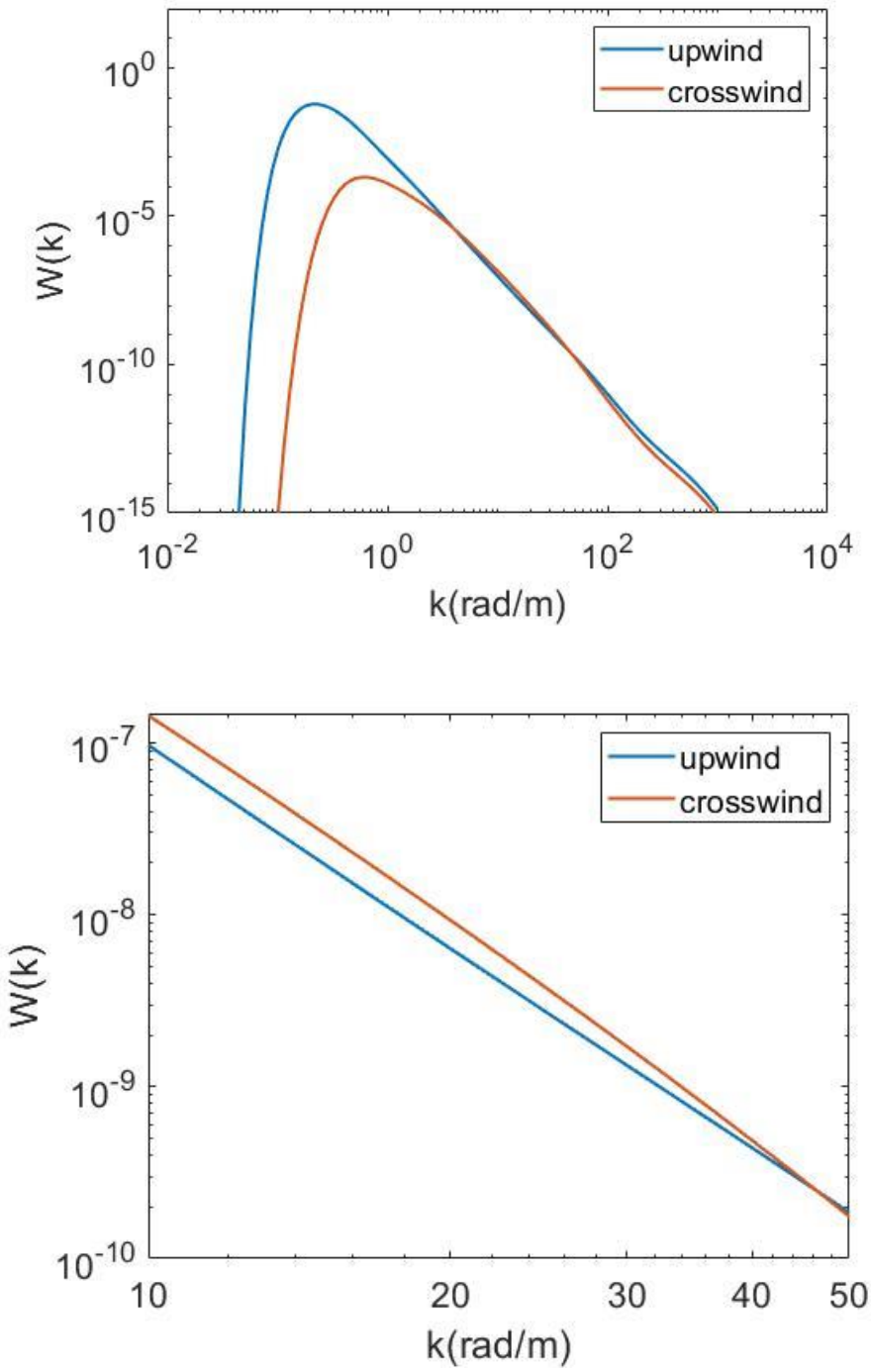

Figure 15 Comparison of upwind and crosswind spectrum with the new spreading function by Du and Apel spectrum for 5m/s. Left figure is the zooming in of the right figure for *k* corresponds to 10 rad/m to 50 rad/m.

Figure 15 shows the Comparison of upwind and crosswind spectrum with the new spreading function by Du and Apel spectrum for 5m/s. It is observed that upwind spectrum is higher than crosswind for whole wavenumber range except for millimeter waves and centimeter waves which corresponds to *k* equal several tens of rad/m.

Even though two kinds of spectrum are used for comparison: Apel and Elfouhaily. The purpose of this chapter is to explore the reason of NUC, and NUC is a comparative relationship between upwind/downwind backscatter and crosswind backscatter. So even though different spectrum will create different absolute VV HH value, we pay more attention on the comparison between upwind and crosswind and also VV/HH ratio.

3.3 Results and discussions

We use two kinds of ocean spectra in this section: Elfouhaily spectrum with or without horseshoe features and Apel spectrum with modified angular spreading function. Three results are compared: experimental data from Aquarius, analytic theoretical results of AIEM and 3D numerical simulations of NMM3D.

Figure 16 shows the in-plane bistatic L-band scattering coefficients at 5 m/s wind speed and 46 degree incidence using Apel spectrum and modified angular spreading function. In these simulations we decompose the bistatic scattering coefficients into coherent and incoherent waves. For the surface sizes used, the coherent waves are only significant in the specular direction while scattering in other directions arises from the incoherent waves. The backscattering direction is highlighted with a dashed line in Figure 16.

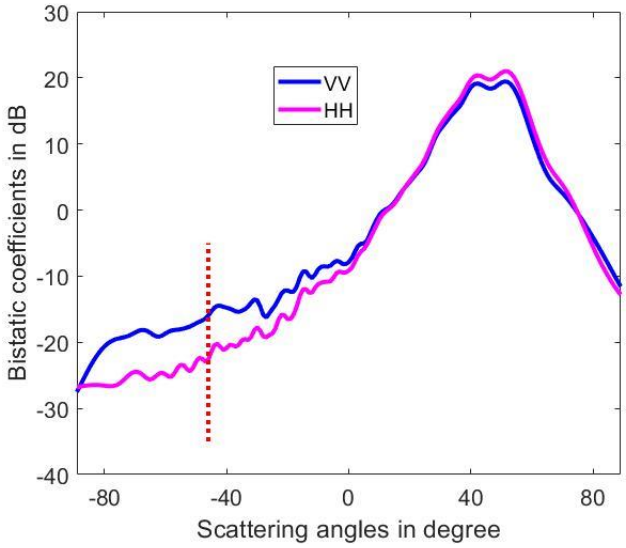

Figure 16 Incoherent bistatic scattering coefficients by NMM3D for 5 m/s at L band using Apel spectrum and modified angular spreading function. Incidence angle is 38 degree.

3.3.1 Scattering of nonlinear Elfouhaily surfaces

Table V VV and HH of surface w/o horseshoe using NMM3D

(a)

upwind	Without horse shoe	With horse shoe
VV	-21.10dB	-20.32dB
HH	-25.53dB	-24.27dB

(b)

crosswind	Without horse shoe	With horse shoe
VV	-25.78dB	-27.24dB
HH	-26.51dB	-29.36dB

The surfaces used in this part are 20 surfaces in a time series: 2 seconds with 0.1 second as the time interval. So in fact there is a close relation between the different surfaces. From the results in Table V we see with or without horseshoe feature, the simulation results do not reproduce NUC.

And also the absolute values of the scattering differ significantly from the Aquarius measurements. This is mostly due to the fact that the 20 surfaces used are closely related to each other.

3.3.2 Scattering of Apel spectra surface with modified angular spreading function

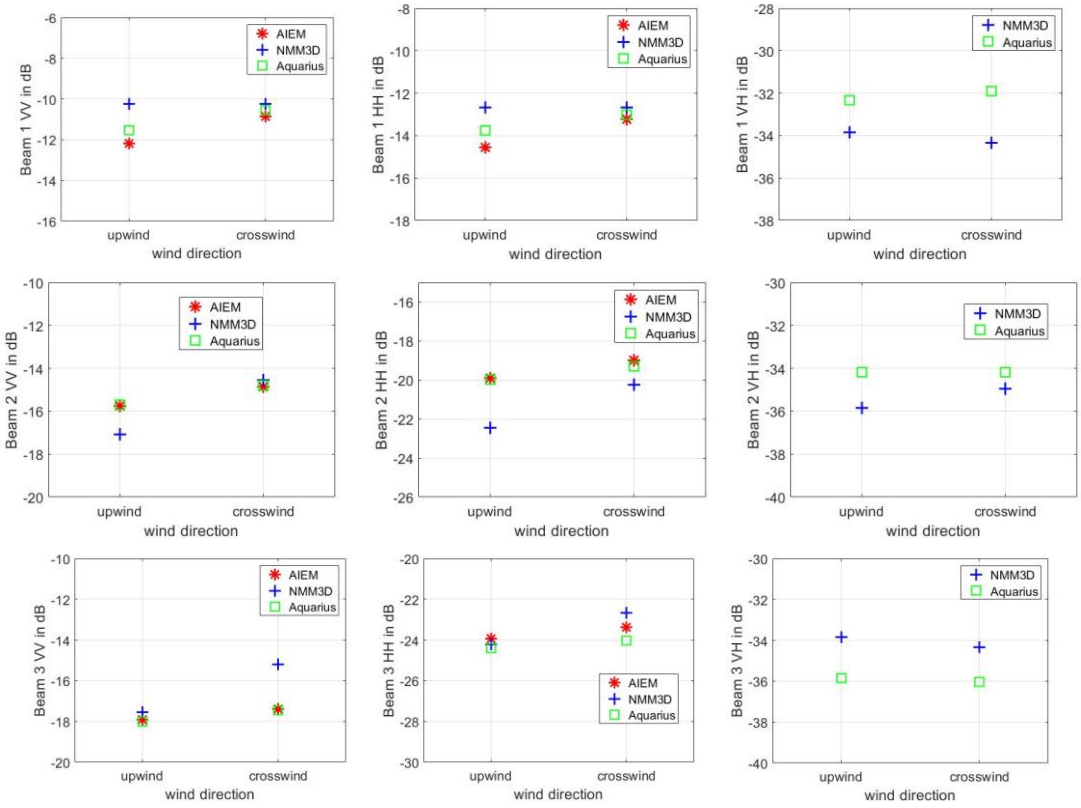

Figure 17 Comparison of backscatters of AIEM, NMM3D, Aquarius at L band for VV, HH and VH for different wind directions. First row: 29° incidence; Second row: 39° incidence; Third row: 46° incidence. The columns are VV HH and VH returns, respectively.

Figure 17 illustrates the results by NMM3D, AIEM, and Aquarius measurement data. The spectrum used in this part is Apel spectrum with the modified ASF described in previous sections. From the figures, we see that the AIEM compared well with Aquarius. This is an obvious conclusion since the new ASF is obtained by data fitting between AIEM and Aquarius. For beam 2 and 3, NMM3D also displays the NUC feature. For beam 1, the like pol of upwind and crosswind are identical to each other. Overall, VV and HH of NMM3D predictions are within 2dB difference

of Aquarius measurement. And the crosspol prediction of NMM3D also has a maximum 2.4dB deviation from Aquarius.

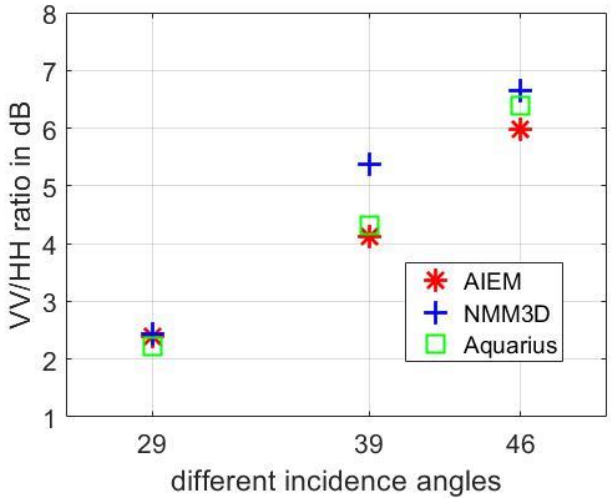

Figure 18 Polarization ratio comparison between NMM3D, AIEM, Aquarius for upwind for the 3 beams: 29°, 39°, 46° at wind speed 5m/s.

Figure 18 plots the polarization ratio of NMM3D, AIEM, Aquarius for the 3 beams of Aquarius. As we can see from Figure 18, the maximum difference for the 29°, 39°, and 46° at wind speed 5m /s is 1dB between NMM3D and Aquarius. Through Figure 17 and Figure 18, we can see that NMM3D predictions are accurate, particularly for cross polarization.

3.4 Conclusions

Recent advances in computers have enabled the simulations of sea surface scattering using numerical method through parallel computing in NMM3D. By implementing moment method with RWG basis functions in surface integral equation, simulation are conducted with the computer generated surface profiles as input. Through this, we are able to test the influence of different scales of ocean waves and different wave patterns on scattering.

Also in this chapter an effort is made to explore the reason for NUC appeared at L band. Through numerical simulations, it is seen that horseshoe patterns cannot generate the NUC

asymmetry at 5m/s. We are proposing a possible reason leading to this: the centimeter waves and millimeter waves are stronger in crosswind than upwind. Through NMM3D simulations, we have seen that Apel spectrum with such a new angular spreading function can lead to backscatter in crosswind exceeding upwind. Thus it is maybe due to the stronger millimeter and centimeter waves at crosswind than upwind that lead to NUC. This is in contrast to one's intuition since wind is blowing in the upwind direction and naturally ocean waves should be stronger in upwind than crosswind. But recent spectrum measurement also shed some light on this reversal [36]. The ocean dynamics is now still being a hot topic due to its complexity.

Up to now, there are various studies about ocean spectra. And the actual process of interaction between electromagnetic waves and ocean surfaces is also quite complicated. We will continue the study of numerical method on wave scattering due to ocean surface.

Chapter 4 Scattering of Lossy Dielectric Surfaces in Full Wave Simulation of Maxwell's Equations with Dense Grid and Neighborhood Impedance Boundary Conditions

4.1 Introduction

Lossy dielectric surfaces are characterized by moderate relative permittivity of about 5 to 80. The imaginary part is smaller than the real part of about 20% to 50% of the real part. Scattering by rough surfaces of these dielectric surfaces are often approximated by perfect electric conductor (PEC) or impedance boundary conditions (IBC). The exact formulation, on the other hand, should be based on dual integral equation with two Green's function g_0 which is the free space Green's function with the wavenumber k of the medium above and g_1 which is the Green's function with the wavenumber k_1 of the lossy dielectric. Compared to IBC or PEC, the dual surface integral equations (SIE) usually have more number of unknowns [47] due to that the unknowns are both electric field and magnetic field on the surfaces. But in order to achieve an accurate results, it is preferable to solve dual surface integral equations rather than solving PEC or IBC which are basically approximations.

For ocean surfaces, as illustrated in Chapter 3, the ocean spectrum is smoother than soil surface. However, compared to soil, the sea water has a much larger permittivity. In previous chapters, the problem under consideration is sea water of permittivity with 75+61i with corresponding complex refractive index 9.26+3.29i. Soil often has a permittivity ranges from 1 to 30. Such a large permittivity of sea water will require a very dense grid to get correct results. This is because the surface electric currents are fluctuating frequently on the surface. The wavelength inside the sea water is around 8 times shorter than that in the air. For PEC scattering problem, 10

points per free space wavelength are usually used in MoM. For lossy dielectric case, if 10 points are used in MoM, this corresponds to we have 1.5 points per wavelength in dielectric medium. Apparently this is not correct. Thus to obtain correct results, around 60~100 points per free space wavelength in discretization of the surface is a must to get correct currents distribution.

Table VI A comparison between PEC, IBC and dual SIE

L=100λ	PEC	IBC	Dual SIE
dielectric	No	Yes	Yes
g_0	Yes	Yes	Yes
g_1	No	No	Yes
Δx	$\frac{\lambda}{10}$	$\frac{\lambda}{10}$	$\frac{\lambda}{64}$
N=number of points	1000	1000	6400
Number of unknowns	1000	1000	12800

In Table VI we are showing a comparison between PEC, IBC and dual SIE for a two dimensional problem. The case is 1 dimensional surface with length L=100λ. For PEC, the dielectric medium is basically considered to be a perfect electric conductor and as is mentioned 10 points per free space wavelength is enough. For IBC, the surface electric field and magnetic field are correlated through a simple relationship and only green function of the air is used. Thus 10 points per wavelength is also enough. For dual SIE, if 64 pints per wavelength is used we will have 12800 number of unknowns. Dual SIE is the only method among the three which has used the green function in the lower medium.

In contrast, in implementation of MoM, in addition to much CPU and memory burden, a tricky problem of slow convergence arises when dense grid is used. With limited computational

resources, it is much preferable to come up with methods to reduce the iterative steps. In computational electromagnetics, 3 methods are mainly used to solve this problem.

1) change basis function
2) use preconditioner
3) use a different equation

In this chapter, we are proposing a novel method to alleviate the problem of slow convergence with dense grid used in scattering of dielectric surfaces. The novel method takes advantages of the fast decaying property of Green function in lower medium along with the propagating distance. This means that if one excite one point on the surface, only nearby points are being influenced due to the fast decaying property of waves in a lossy medium. The band nature relating fields to each other is utilized and is further found to lead to a fast convergence. Compared to IBC which local electric field and magnetic field are related by a simple relationship of approximation, this new method exploits the band nature of green function and formulates the correct relationship of surface electric field and magnetic fields. We name this method the Neighborhood Impedance Boundary Condition (NIBC). Through our results, it is shown that NIBC is both stable and accurate for different wind speeds and can also be applied to 3D problems. Combined with fast algorithm, NIBC can be both computational fast and efficient.

The permittivity used in this chapter are $75+61i$ except otherwise indicated. Ocean spectrum of Pierson-Moskowitz is used. The chapter is organized as follows: in section 4.2, we are presenting the integral equations used. A tapered incidence wave is also introduced. In 4.3, Pierson-Moskowitz is described. This is followed up with the introduction of NIBC method. Then in the final results and discussion part, first we will show that dual SIE is more accurate than IBC. Then it is proved that dense grid is needed for lossy medium to achieve correct results. Then a slow convergence problem is described when dense grid is implemented compared to coarse grid.

Finally, we will show that NIBC can alleviate the slow convergence problem but at the same time can be both accurate and stable.

4.2 Formulations

In this section, we will introduce the formulations used in IBC and dual SIE. Also tapered wave incidence is described in this section.

4.2.1 Dual surface integral equation

For the 2D rough surface scattering problem, the governing dual surface integral equation (SIE) derived from extinction theorem from both air and medium are [49]

$$-\int dx'\left[\psi(x')\sqrt{1+\left(f'(x')\right)^2}\,\frac{\partial}{\partial n'}g(x,z;x',z')-g(x,z;x',z')u(x')\right]_{z'=f(x')}=\psi_{inc}(x,z) \quad (55)$$

$$-\int dx'\left[\psi(x')\sqrt{1+\left(f'(x')\right)^2}\,\frac{\partial}{\partial n'}g_1(x,z;x',z')-g_1(x,z;x',z')\frac{1}{\rho}u(x')\right]_{z'=f(x')}=0 \quad (56)$$

$$u(x)=\sqrt{1+\left(f'(x)\right)^2}\,\frac{\partial}{\partial n}\psi(x) \quad (57)$$

where $g(x,z;x',z')$ is Green function in the air which is $\frac{i}{4}H_0^{(1)}(k\rho)$. k is the wavenumber in the air. $g_1(x,z;x',z')$ is Green function in the lower medium which is $\frac{i}{4}H_0^{(1)}(k_1\rho)$. k_1 is the wavenumber in the lower medium. Ψ is the electric field if it is TE polarization and is magnetic field if it is TM polarization.

$$\begin{aligned} k &= \omega\sqrt{\mu\varepsilon} \\ k_1 &= \omega\sqrt{\mu_1\varepsilon_1} \end{aligned} \quad (58)$$

$f(x)$ is the rough ocean surface profile and $f'(x)$ is the slope of the surface. $\hat{n}$ is the normal vector of the surface. ψ and u are surface fields. And ρ is an indicator of TE and TM incidence. ψ_{inc} is the incidence wave. Then after performing point matching to the above two equation, we get

$$\bar{\bar{A}}\bar{u} + \bar{\bar{B}}\bar{\psi} = \bar{\psi}_{inc} \tag{59}$$

$$\bar{\bar{A}}_1\bar{u} + \bar{\bar{B}}_1\bar{\psi} = 0 \tag{60}$$

For matrix elements in (59), we have

$$A_{mn} = g\left(x_m, z_m; x_n, z_n\right)\Delta x \quad \text{for } m \neq n \tag{61}$$

$$A_{mm} = \frac{i}{4}\Delta x\left[1 + i\frac{2}{\pi}\ln\left(\frac{\gamma k \Delta x}{4e}\sqrt{1+\left(f'\left(x_m\right)\right)^2}\right)\right] \tag{62}$$

$$B_{mn} = -\Delta x\sqrt{1+\left(f'\left(x_m\right)\right)^2}\left[\frac{\partial}{\partial n'}g\left(x_m, z_m; x', z'\right)\right] \quad \text{for } m \neq n \tag{63}$$

$$B_{mm} = \frac{1}{2} \tag{64}$$

For matrix elements in (60), we have

$$A_{mn,1} = g_1\left(x_m, z_m; x_n, z_n\right)\Delta x \quad \text{for } m \neq n \tag{65}$$

$$A_{mm} = \frac{i}{4}\Delta x\left[1 + i\frac{2}{\pi}\ln\left(\frac{\gamma k_1 \Delta x}{4e}\sqrt{1+\left(f'\left(x_m\right)\right)^2}\right)\right] \tag{66}$$

$$B_{mn,1} = -\Delta x\sqrt{1+\left(f'\left(x_m\right)\right)^2}\left[\frac{\partial}{\partial n'}g_1\left(x_m, z_m; x', z'\right)\right] \quad \text{for } m \neq n \tag{67}$$

$$B_{mm} = -\frac{1}{2} \tag{68}$$

For usual perfect electric conductor (PEC) scattering problem, 10 points per free space wavelength is usually enough to get correct results. But for dielectric medium with a large permittivity 10 points per wavelength is far from enough. A usual criteria is to discretize the gird so that there are around 10 points per medium wavelength.

4.2.2 Impedance boundary condition

For the assumption of impedance boundary condition, the surface electric field and surface magnetic field is related through the following relationship

$$\bar{E}\,|_{\tan} = Z_s \hat{n} \times \bar{H} \tag{69}$$

where Z_s is the impedance of the lower medium.

For two dimensional problem, we have

$$\frac{1}{i\omega\varepsilon}\left(\hat{n}\cdot\nabla\psi\right) = -Z_s\psi = \frac{1}{i\omega\varepsilon}\frac{u}{\sqrt{1+\left(f\left(x\right)\right)^2}} \quad \text{for TM polarization} \tag{70}$$

$$\frac{1}{i\omega\mu}\left(\hat{n}\cdot\nabla\psi\right) = -Z_s\psi = \frac{1}{i\omega\mu}\frac{u}{\sqrt{1+\left(f\left(x\right)\right)^2}} \quad \text{for TE polarization} \tag{71}$$

Thus for either TM or TE polarization we can substitute (70) or (71) into equation (55) to get a simplified equation which only has one kind of unknowns.

4.2.3 Tapered incidence wave

Similar to 3D problems, a tapered incident wave is used in the simulation due to the fact that the surface has to be truncated to a finite length of *L*. To avoid artificial edge diffraction, the tapered incident wave is defined as

$$\psi_{inc}(x,z)=\exp\left(ik\left(x\sin\theta_i-z\cos\theta_i\right)\left(1+w\right)\right)\exp\left(-\frac{\left(x+z\tan\theta_i\right)^2}{g^2}\right)^2 \tag{72}$$

where g is the tapering parameter and

$$w=\frac{2\frac{\left(x+z\tan\theta_i\right)^2}{g^2}-1}{\left(kg\cos\theta_i\right)^2} \tag{73}$$

The incident wave is close to a plane wave for large surface length L. The tapering parameter is taken as $g = L/4$.

4.3 Pierson-Moskowitz spectrum

As a function of wavenumber, gravity and wind speed the form of Pierson-Moskowitz spectrum is [14]

$$W_{PM}(k,\phi)=\frac{a_0}{2k^4}\exp\left(-\frac{\beta g^2}{k^2U_{19.5}^4}\right)\Phi(k,\phi) \tag{74}$$

where $a_0 = 0.0081, \beta = 0.74$, g is the gravitational acceleration equation to 9.81 m/sec^2. And $U_{19.5}$ is the wind speed at the altitude of 19.5 m above the mean sea level. In (74), $\Phi(k,\phi)$ is the directional factor. But since we are exploring the two dimensional problem, $\Phi(k,\phi)$ is set to be 1 in this chapter.

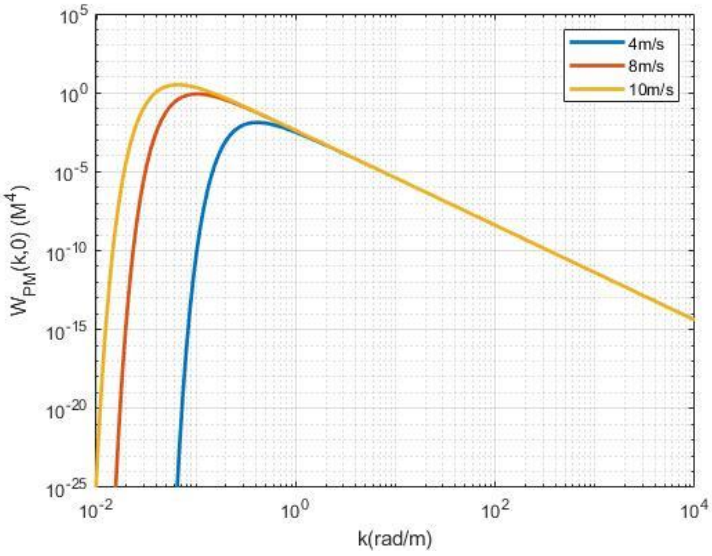

Figure 19 Amplitude of the Pierson-Moskowitz spectrum for along-wind direction and wind speeds $U_{19.5}$=4, 8 and 10 m/s

Figure 19 plots the amplitude of the Pierson-Moskowitz spectrum for along-wind direction and wind speeds $U_{19.5}$=4, 8 and 10 m/s. It is seen that much of the energy is concentrated on small wavenumber. And with an increase of wind speed, the peak of the spectrum is moving towards the small wavenumber. This means that longer ocean waves are included in higher wind speeds.

4.4 Neighborhood impedance boundary condition

In this section we are describing the proposed novel method for scattering of highly dielectric lossy surfaces. Different from usual method which solves (59) and (60) directly, the proposed NIBC method is trying to solve (60) first. We then have

$$\bar{u} = -\bar{\bar{A}}_1 \bar{\bar{B}}_1 \bar{\psi} = \bar{\bar{M}} \bar{\psi} \tag{75}$$

$\bar{\bar{M}}$ is the matrix relating $\bar{u}$ and $\bar{\psi}$ which is in contrast to the relationship defined in (70) and (71).Substitute (75) into (59), gives

$$\left(-\bar{\bar{A}} \bar{\bar{A}}_1^{-1} \bar{\bar{B}}_1 + \bar{\bar{B}} \right) \bar{\psi} = \bar{\psi}_{inc} \tag{76}$$

(76) then becomes the final equation we are solving. In the above procedure, we are facing the following 3 issues.

A. Inversion of matrix $\bar{\bar{A}}_1$

As mentioned earlier, since the permittivity of sea water has a large imaginary part, the waves will decay fast with the travelling distance. Thus the matrix $\bar{\bar{A}}_1 \; and \; \bar{\bar{B}}_1$ are actually band matrix. We can set up a bandwidth *BW* of the matrices that the matrix entries outside the *BW* is set to be zero.

Figure 20 shows a comparison of 3D green function of air and sea water in terms of absolute value. It is easy to see that the green function in the sea water decays very fast. Even for a propagating distance of one λ, the absolute value drops to 10^{-10} which is much lower than the green function in the air. This means that $\bar{\bar{A}}_1 \; and \; \bar{\bar{B}}_1$ actually behaves like a band matrix. The matrix elements quickly decrease when moving away from the diagonal line.

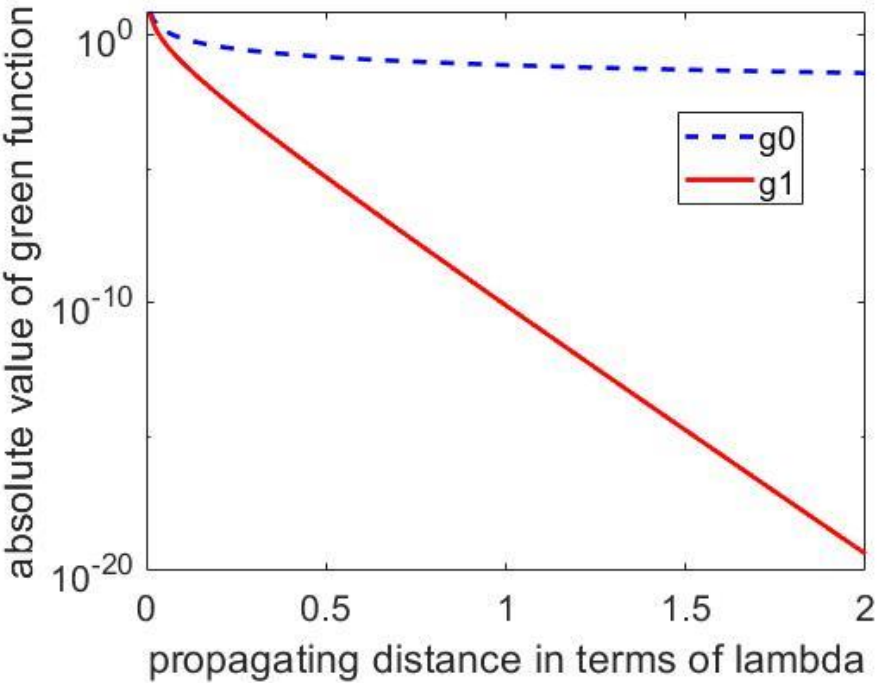

Figure 20 3D Green function comparison of air and sea water as a function of propagating

In our numerical implementation, the *BW* is configured that the furthest elements in the matrix are 10^{-4} lower than the diagonal part. It is observed that when BW equal $\frac{1}{4}\lambda$ can meet such a requirement. In the results section, we will show that the accuracy varies little with the *BW* used in the simulation. Now the problems reduces to solve for the inverse matrix of a diagonal matrix with a bandwidth *BW*. The following is an expression of the definition of inversion.

$$\bar{\bar{A}}_1 \bar{\bar{A}}_1^{-1} = \bar{\bar{I}} \tag{77}$$

In order to obtain the inverse of $\bar{\bar{A}}_1$, we can solve for each column of $\bar{\bar{A}}_1^{-1}$ one at a time. That is each time we are solving

$$\bar{\bar{A}}_1 \bar{a}_n = \bar{e}_n \tag{78}$$

where $\bar{a}_n$ is the nth column of matrix $\bar{\bar{A}}_1$ and $\bar{e}_n$ is a column vector with all zero elements except the nth element.

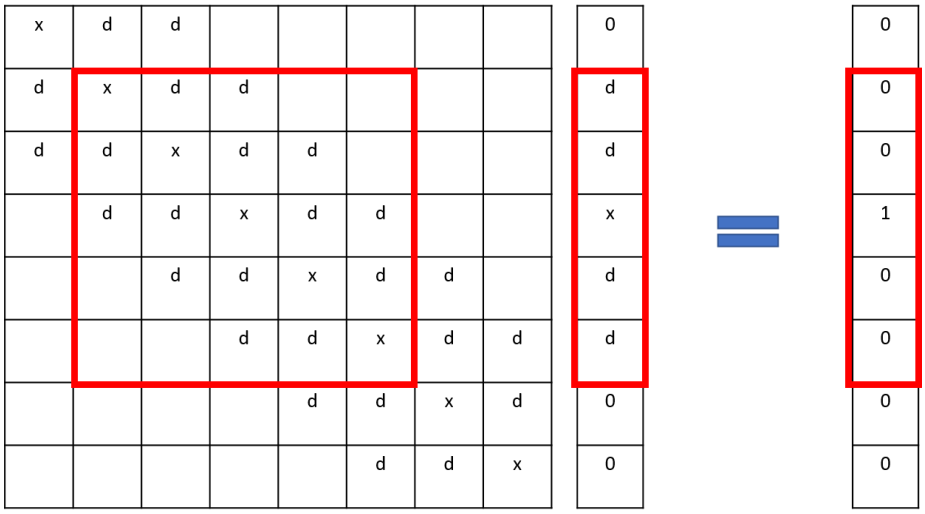

Figure 21 Fast method for band matrix inversion

Figure 21 shows an example about how we invert the matrix. In this case, the *BW* is 3 grids and the figure is showing a case to solve for the 4th column of the matrix $\bar{\bar{A}}_1^{-1}$. Then we just need to solve an inversion problem of size 5 by 5. The '*x*' and '*d*' in the figure represent diagonal and off-diagonal elements, respectively. Thus compared to usual method of inversing a matrix which is of the computation complexity order $O(N^3)$, our method will only require $O(N \cdot BW^3)$.

B. Computation of $\bar{\bar{A}}_1^{-1}\bar{\bar{B}}_1\bar{b}$

$\bar{\bar{A}}_1^{-1}$ and $\bar{\bar{B}}_1$are both band matrix with bandwidth around *BW*. We can do first step

$$\bar{\bar{B}}_1\bar{b} = \bar{c} \tag{79}$$

The computational complexity is of order $\mathrm{O}(N \cdot \mathrm{BW})$. Then

$$\bar{\bar{A}}_1^{-1}\bar{c} = \bar{d} \tag{80}$$

The computational complexity is also of order $O(N \cdot \mathrm{BW})$. Thus a nice feather of band matrix is that it is not so computation expensive while conducting matrix vector multiplication.

C. $\bar{\bar{A}}\bar{b}$ and $\bar{\bar{B}}\bar{b}$

We have implemented PBTG/SMCG to accelerate this part. The details are described in the next chapter.

When doing matrix times vector, since $\bar{\bar{B}}_1$, $\bar{\bar{A}}_1^{-1}$ are set to be band matrix, only entries within the bandwidth need to be calculated and stored. This has in fact reduced the memory storage.

4.5 Results and Discussions

There are 3 methods in this section: IBC, NIBC, and benchmark solutions. Benchmark solutions refer to the results by directly solving equations (59) and (60). All the cases in this section

are TM incidence cases except otherwise indicated. The dielectric constant is 75+61i and the MoM is conducted on a mesh with 64 points per free space wavelength. The ocean spectrum of Pierson Moskowitz spectrum is used. The error of using Frobenius norm is used to calculate the difference between two arrays. It is defined as

$$error = \frac{\|array1 - array2\|_F}{\|array1\|_F} \tag{81}$$

where $\|\quad\|_F$ is the Frobenius norm

$$\|C_{n\times 1}\|_F = \sqrt{\sum_{i=1}^{n} |c_i|^2} \tag{82}$$

4.5.1 Comparison between IBC and benchmark solution

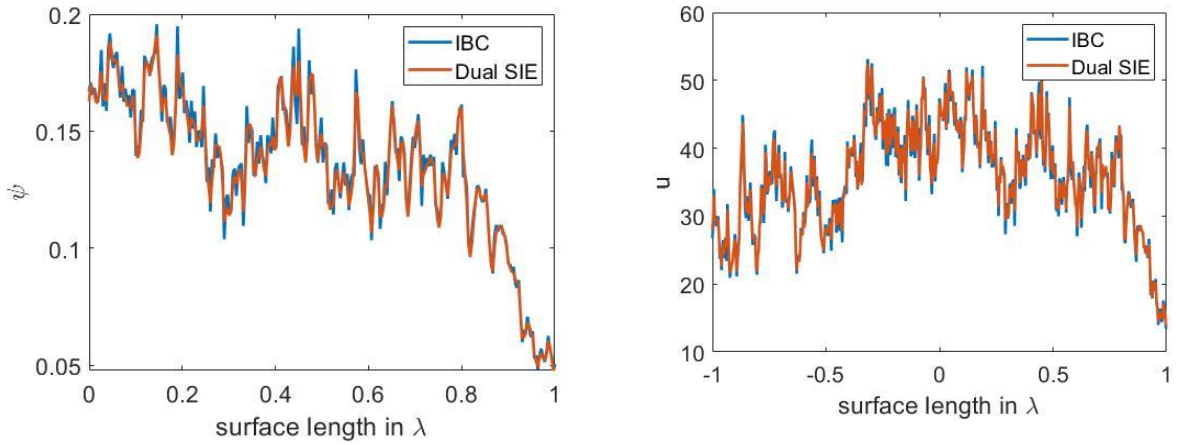

Figure 22 Surface fields comparisons between IBC and benchmark solution for TE incidence at 5m/s.

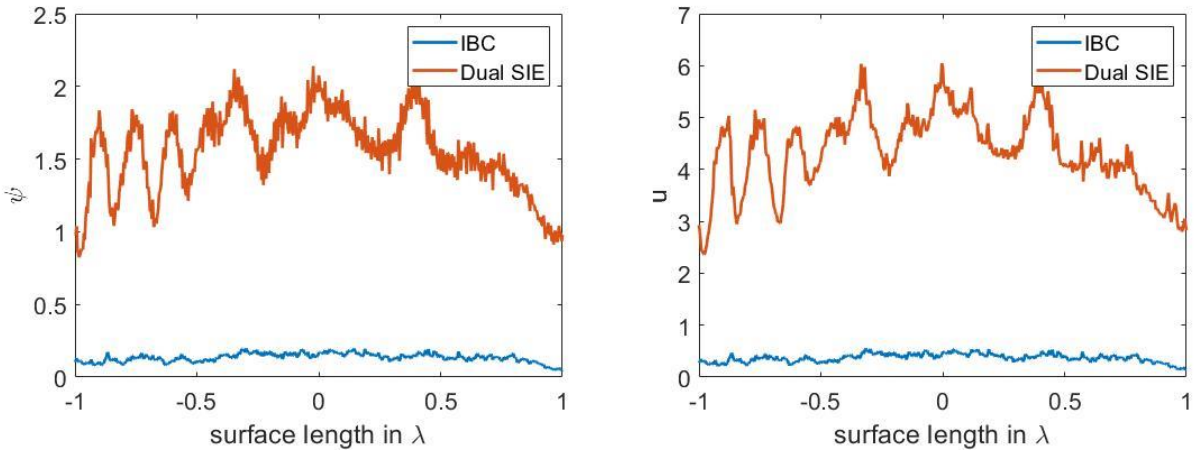

Figure 23 Surface fields comparisons between IBC and benchmark solution for TM incidence at 5m/s

In Figure 22 and Figure 23, we are plotting the surface fields comparisons between IBC and benchmark solution for TE and TM incidence at 5m/s, respectively. Red curved are benchmark while blue curves are IBC. The *x* axis is the surface in terms of λ. The *y* axis is the amplitude of surface fields. The discretization used is $\Delta x = \frac{1}{64}\lambda$. We can see that IBC for TE case is closer to benchmark than TM case. And also IBC has a minimum difference of 5% difference compared to benchmark solution. In order to correctly simulate the scattering problem of lossy medium, dual SIE must be solved.

4.5.2 Single dense grid and single coarse grid

In this chapter, we have used SCG for single coarse grid (around 10 points per free space wavelength), SDG for single dense grid (60 points or more per free space wavelength) which are the same as in Li's paper [48].

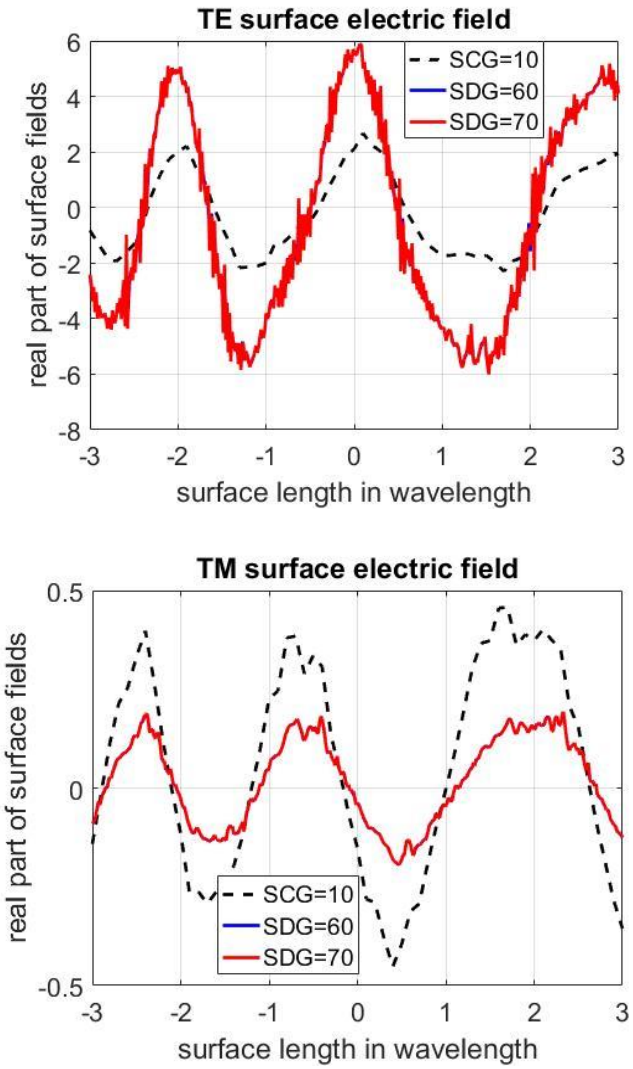

Figure 24 Comparison of surface currents for SDG and SCG.

Figure 24 shows the comparison of surface electric fields for both TE and TM case for different discretization density using the same surface profile. The *x* axis is the surface length in wavelength. The *y* axis is the value of electric field on the surface. Both figures indicate that 60 points per wavelength match well with 70 points per wavelength and are quite different with the coarse grid which is 10 pints per wavelength. This means that for a dielectric surface with a large permittivity, it is desired to use dense grid up to 60 points per free space wavelength to get converged surface currents distribution.

4.5.3 Slow convergence of dense grid

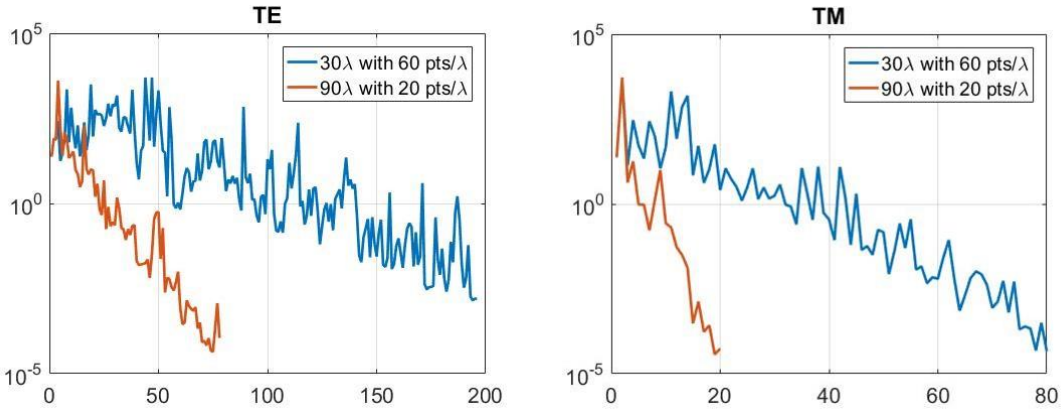

Figure 25 Residual error changing with iterations for two kinds of surfaces: 30λ long surface with 60 points/ λ (blue curve) and 90 λ long surface with 20 points/ λ (red curve) for both TE (left figure) and TM incidence (right figure).

As mentioned earlier, the dense grid will bring up the slow convergence problem.

Figure 25 shows the residual error along with iterative steps produced by conjugate gradient method for two kinds of surfaces: 30λ long surface with 60 points/ λ and 90 λ long surface with 20 points/ λ for both TE and TM incidence. It is seen that the two cases have the same number of unknowns. But apparently the dense grid case converges much slowly that the coarse grid case. This phenomenon has also been found in 3D problem case: the dense grid always converge much slowly than coarse grid case. The proposed new method in this chapter is now implemented onto 2D problems. But it can also be applied to 3D problems.

4.5.4 NIBC for alleviating numerical issues brought by dense grid

In Figure 26, we are plotting the error of matrix $\bar{\bar{M}}$ in terms of Frobenius norm. $\bar{\bar{M}}$ is relating surface magnetic field and surface electric field and is defined in equation (75). For IBC, the matrix $\bar{\bar{M}}$ is simply a diagonal matrix due to the definition of IBC as defined in equation (70) and (71). The top figure is the ocean surfaces and bottom figure is the soil surface characterized

by exponential correction function. From Figure 26 we see that the error of IBC is less than 0.1% while the error norm for IBC is more than 80%.

Figure 27 shows the comparison of surface fields errors of IBC and NIBC compared to benchmark solutions. The red lines are surface fields calculated by NIBC and black lines are IBC. It is also observed that the error norm of IBC is less than 0.1% for both ocean and soil surfaces while IBC has an error norm of more than 1% for ocean surfaces and 10% for soil surfaces.

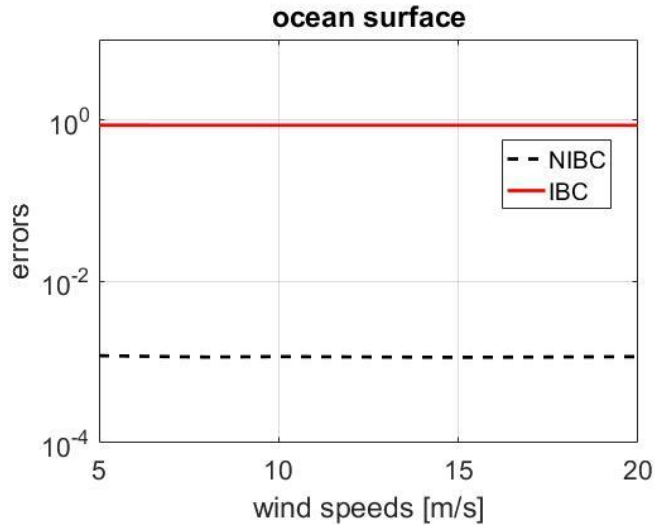

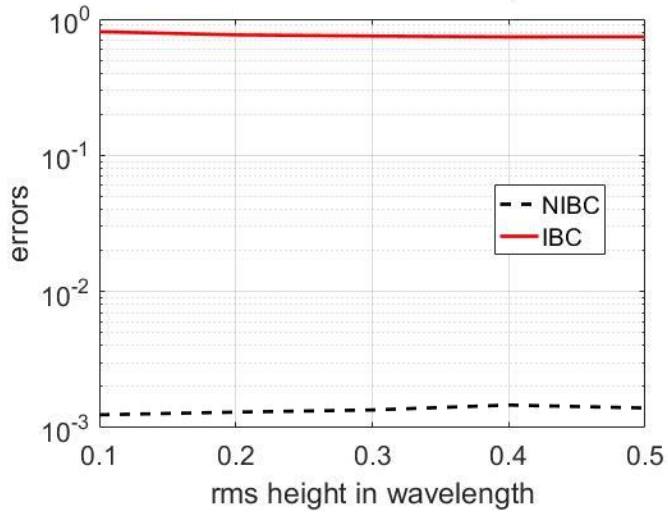

Figure 26 Comparison of matrix $\bar{\bar{M}}$ between NIBC and IBC with benchmark method (top) ocean surface (bottom) soil surface

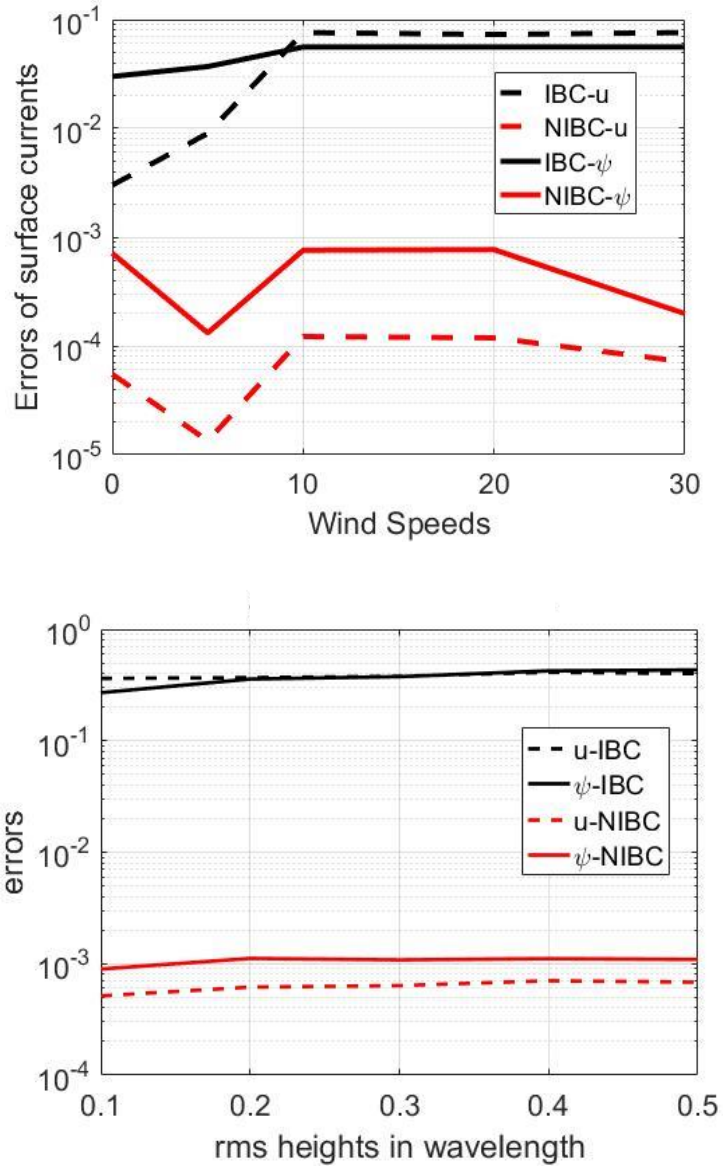

Figure 27 Surface fields errors of IBC and NIBC compared to benchmark solution (top) ocean surface (bottom) soil surface

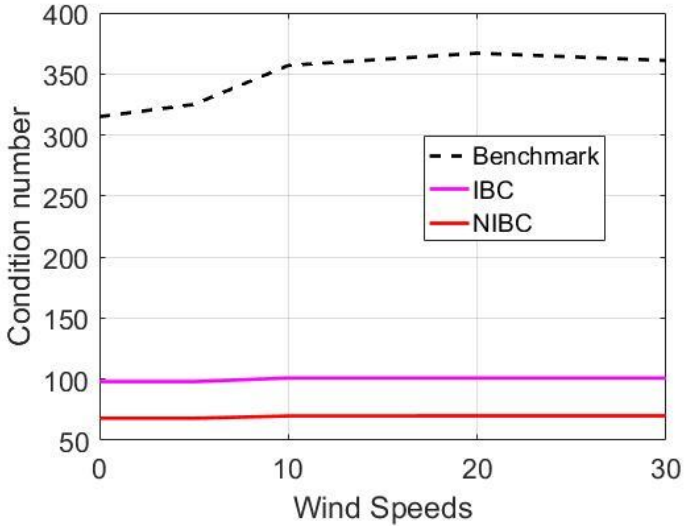

Figure 28 Condition number comparison for IBC, NIBC, and benchmark method for ocean surfaces

We plot the condition number comparison for IBC, NIBC, and benchmark method for ocean surfaces in Figure 28. It is seen that the NIBC has a much smaller condition number than IBC and benchmark solution. Thus NIBC has actually changed the property of the impedance matrix.

4.6 Conclusions

In this chapter, I am trying to show that

1) Dual SIE must to be solved instead of IBC or PEC to get correct scattering results

2) Dense grid is needed to obtain correct results for medium with a large permittivity

3) The proposed NIBC is an efficient way to reduce slow convergence rate brought by dense grid

With a high dielectric constant, a dense grid as up to 64 points per wavelength is necessary to get correct results by using Method of Moments. Rigorous solution of solving Maxwell Equation will result in a high CPU and memory consumption with such a dense grid. What is more, the

impedance matrix is usually ill conditioned which needs plenty of iterative steps to get converged. The proposed NIBC method exploits the band nature of the impedance matrix formulated by the extinction theorem in the lower medium and can produce exact solution of the problem even for high winds. Through our numerical results, we found the errors of NIBC is controllable and used less CPU and memory. NIBC is also quite stable for different wind speeds and even soil surfaces.

Chapter 5 Fast Computational Method of Combing Low Rank Property and SMCG for Scattering of Ocean Surfaces

5.1 Introduction

As mentioned in chapter 4, a set of dense grid is needed to get the correct current distribution of a highly lossy surface. This is due to the fact that Green function of lower medium is changing rapidly and wavelength in the lower medium is much smaller than that in the air. But on the other hand, the green function in the air is slow varying. If we use single dense grid for both green functions in the air and medium, CPU and memory consumption will be quite a lot. This has become the incentives of this chapter: to finally achieve that dense grid is used in the lower medium while coarse grid is used in the upper medium.

In chapter 4, we proposed a new method to accelerate the convergence rate in the iterative solver. The new method is termed as Neighborhood Impedance Boundary Condition (NIBC). The final equation to be solved is

$$\left(-\bar{\bar{A}}\bar{\bar{A}}_1^{-1}\bar{\bar{B}}_1+\bar{\bar{B}}\right)\bar{\psi}=\bar{\psi}_{inc} \tag{83}$$

In this equation $\bar{\bar{A}}$ and $\bar{\bar{B}}$ are only related to Green function in the upper medium. $\bar{\bar{A}}_1$ and $\bar{\bar{B}}_1$ are related to Green function in the lower medium. And in chapter 4, dense grid as large as 64 points per wavelength is used to form the matrices of $\bar{\bar{A}}$, $\bar{\bar{B}}$, $\bar{\bar{A}}_1$ and $\bar{\bar{B}}_1$. But according to our analysis only $\bar{\bar{A}}_1$ and $\bar{\bar{B}}_1$ are required to use dense grid.

On the hand, the far field interaction displays low rank property. We will use the following example to show this property.

The rough surface is a 32λ long surface, and each λ we define as a block (patch) with 64 discretization points. Then we have 32×32 interaction submatrix to form the matrix $\bar{\bar{A}}$. For near field interaction, e.g. the interaction of block itself, the submatrix is a full rank matrix. But when the field and source block are distant from each other, it is found that the submatrix is low rank.

In Figure 29 we are showing the rank comparison between the rough surface we mentioned and the flat surface. Source patch is 16th patch and field patch is ranging from 1 to 32. It is seen that the self-interaction matrix which corresponds to the middle point of the figure is full rank which is 64 due to the fact that there are 64 points per wavelength. On the other hand, we see that the rank drops quickly with the distance between the source patch and field patch. Also, it is observed that the flat surface typically has a lower rank compared to the rough surface.

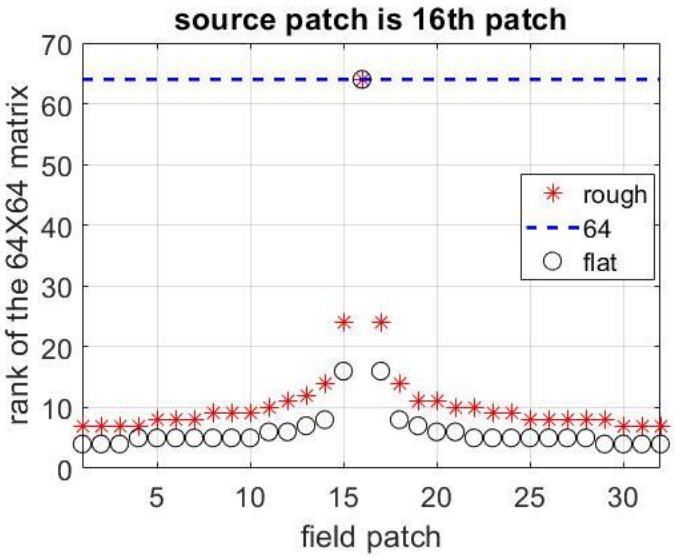

Figure 29 Rank comparison for rough surface and flat surface. Source patch is 16th patch and field patch is from 1 to 32

The low rank property has been utilized in UV method to accelerate the matrix vector multiplication by Tsang [48]. Here we propose another fast computation method based on Steepest Descent Method (SDM) to combine the low rank property and SMCG. In the following sections,

64 points is used for green function in the lower medium which are basically $\bar{\bar{A}}_1$ and $\bar{\bar{B}}_1$. But utilizing our method it is achieved that 8 points per free space wavelength are used in $\bar{\bar{A}}$, $\bar{\bar{B}}$. This method can also be applied to 3D problems.

5.2 Formulation

In this section, the formulation of combining PBTG and SMCG is illustrated.

In the up medium, we have Green function defined as:

$$g\left(\bar{r},\bar{r}'\right)=\frac{i}{4}H_0^{(1)}\left(k\left|\bar{r}-\bar{r}'\right|\right) \tag{84}$$

Then we put it in a form of plane summation.

$$g\left(x,z\right)=\frac{i}{4}\int_{-\infty}^{\infty}dk_z\exp^{ik_x|x|}\exp^{ik_z z}\frac{1}{z} \tag{85}$$

Later on $x\to x-x',z\to z-z'$.

The integration contour is on the real k_z axis. Next we make transformation to complex angle.

$$\begin{aligned}k_z&=k\cos\alpha=k\cos(\alpha'+i\alpha'')=k_{z'}+ik_{z''}\\k_x&=k\sin\alpha\end{aligned} \tag{86}$$

Balancing real and imaginary parts

$$\begin{aligned}k_{z'}&=k\cos\alpha'\cosh\alpha''\\k_{z''}&=-k\sin\alpha'\sinh\alpha''\end{aligned} \tag{87}$$

Similarly for k_x

$$k_{x'}+ik_{x''}=k\sin\alpha'\cosh\alpha''+ik\cos\alpha'\sinh\alpha'' \tag{88}$$

we also have $dk_z=-k\sin\alpha d\alpha$.

The original contour integral is now in the complex α plane and is denoted the Sommerfeld integration path (SIP):

$$g(x,z)=\frac{i}{4\pi}\int_{\mathrm{SIP}} d\alpha \exp^{ik|x|sin\alpha+ikzcos\alpha} \tag{89}$$

The Sommerfeld integration path extends from $\alpha=0+i\infty$. to $\alpha=0$ along the imaginary axis. It then goes from $\alpha=0$ to $\alpha=\pi$ along the real α axis. Finally it goes from $\alpha=\pi$ to $\alpha=\pi-i\infty$. Since $|x|>>|z|$, the dominant exponential term is

$$\begin{aligned} e^{ik|x|sin\alpha} &= e^{i(k|x|sin\alpha' cosh\alpha''+ik|x|cos\alpha' sinh\alpha'')} \\ &= e^{ik|x|-k|x|cos\alpha' sinh\alpha''} \end{aligned} \tag{90}$$

The steepest descent path Γ is defined by

$$\begin{aligned} &\Re(\sin\alpha)=1 \\ &sin\alpha' cosh\alpha''=1 \end{aligned} \tag{91}$$

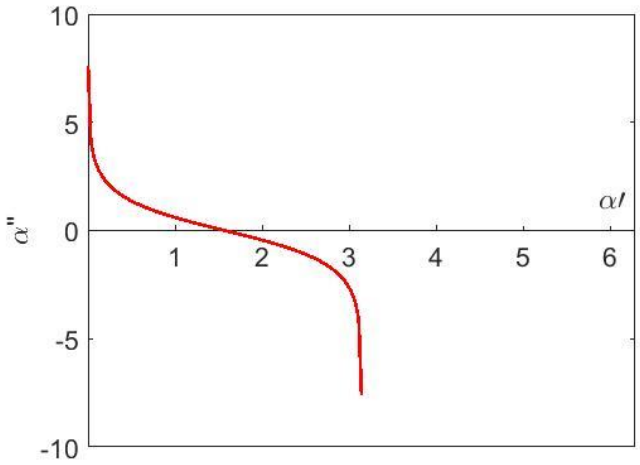

Figure 30 Steepest descent path and Sommerfeld integration path (SIP)

Figure 30 plots the steepest descent path for the integral appeared in (89). The steepest descent path means that the integral converge fastest through this path.

The saddle point is at $\alpha = \pi / 2$. The steepest descent path Γ is a contour of constant phase for the dominant exponential term, the amplitude of which decreases rapidly away from the saddle point. Then solving (89) using the numerical quadrature along the steepest descent path, we have

$$\begin{aligned} g(x,z) &= \frac{i}{4\pi}\int_{\Gamma} d\alpha e^{ik|x|\sin\alpha + ikz\cos\alpha} \\ &= \frac{i}{4\pi}\sum_{q=1}^{Q} e^{ik|x|\sin\alpha_q + ikz\cos\alpha_q}\Delta\alpha_q \end{aligned} \tag{92}$$

Let $\alpha_{q\_new} = \pi - \alpha$ and then let $\alpha_{q\_new} \to \alpha$, we have

$$\begin{aligned} g(x,z) &= \frac{i}{4\pi}\int_{\Gamma} d\alpha e^{ik|x|\sin\alpha - ikz\cos\alpha} \\ &= \frac{i}{4\pi}\sum_{q=1}^{Q} e^{ik|x|\sin\alpha_q - ikz\cos\alpha_q}\Delta\alpha_q \end{aligned} \tag{93}$$

The above can use FFT to accelerate, e.g.

$$\begin{aligned} g(x,z) &= \frac{i}{4\pi}\sum_{q=1}^{Q} e^{ik|x-x'|\sin\alpha_q - ik(z-z')\cos\alpha_q}\Delta\alpha_q \\ &= \frac{i}{4\pi}\sum_{q=1}^{Q} e^{-ikz\cos\alpha_q} e^{ik|x-x'|\sin\alpha_q}\Delta\alpha_q e^{ikz'\cos\alpha_q} \end{aligned} \tag{94}$$

In equation(94), we have separate apart x, x' with z, z'. Since x, x' are defined on canonical grid, we can accelerate the multiplication of (94) with a column vector through FFT which is similar to SMCG. To determine α_q, we have used the method present in [14]. Let BW be the bandwidth on either side of $\alpha' = \frac{\pi}{2}$. We sample evenly on the α' axis with interval $\Delta\alpha'$. Let the number of angles Q be an odd integer. Then

$$\Delta\alpha' = \frac{2(BW)}{Q-1} \tag{95}$$

$$\alpha_q = \alpha_q' + i\alpha_q'' \tag{96}$$

$$\alpha'_q = \frac{\pi}{2} - (BW) + (q-1)\Delta\alpha' \tag{97}$$

$$\cosh\alpha''_q = \frac{1}{\sin\alpha'_q} = \frac{1}{\cos\beta} \tag{98}$$

It is required that

$$kx_{\min}(BW)^2 \gg 1 \tag{99}$$

$$BW = \frac{C_l}{\sqrt{kx_{\min}}} \quad (C_l = \text{large constant}) \tag{100}$$

where x_{min} is the minimum separation in *x*. It is also required that

$$kx_{\max}(\Delta\alpha')^2 \ll 1 \tag{101}$$

$$\Delta\alpha' = \frac{C_s}{\sqrt{k|x_{\max}|}} \quad (C_s = \text{small constant}) \tag{102}$$

where x_{max} is the maximum separation in *x*. In our numerical implementation we have

$$\begin{aligned} C_l &= 3 \\ C_s &= \frac{1}{3} \end{aligned} \tag{103}$$

Then

$$Q \simeq \frac{2C_l}{C_s}\sqrt{\frac{x_{\max}}{x_{\min}}} \tag{104}$$

Further, suppose $x > x'$

$$\begin{aligned} &g(x,z;x',z') \\ &= \frac{i}{4\pi}\sum_{q=1}^{Q} e^{ik(x-x_f)\sin\alpha_q - ikz\cos\alpha_q} e^{ik(x_f-x_s)\sin\alpha_q} \Delta\alpha_q e^{-ik(x'-x_s)\sin\alpha_q + ikz'\cos\alpha_q} \end{aligned} \tag{105}$$

To deal with the gradient green function, we can use the property of Bessel function

$$J_0^1 = -J_1 \tag{106}$$

In the above equation, *J* stands for all Bessel functions. For the kernel of Gradient Green function, we have

$$\sqrt{1+\left(\frac{df'(x')}{dx'}\right)^2}\,\hat{n}'\cdot\nabla' g = \left(\hat{z}-\frac{df'(x')}{dx'}\hat{x}\right)\cdot\nabla' g \tag{107}$$

$$\begin{aligned}\nabla' g &= \frac{i}{4}\nabla' H_0^{(1)}\left(k\sqrt{(x-x')^2+(z-z')^2}\right)\\ &= \frac{i}{4\pi}\nabla'\sum_{q=1}^{Q} e^{-ikz\cos\alpha_q}e^{ik|x-x'|\sin\alpha_q}\Delta\alpha_q e^{ikz'\cos\alpha_q}\\ &= \frac{i}{4\pi}\sum_{q=1}^{Q}\left(\pm\hat{x}ik\sin\alpha_q+\hat{z}ik\cos\alpha_q\right)e^{-ikz\cos\alpha_q}e^{ik|x-x'|\sin\alpha_q}\Delta\alpha_q e^{ikz'\cos\alpha_q}\end{aligned} \tag{108}$$

Also suppose $x' > x$, then use + sign in the equation. If $x' < x$, then - sign

$$\begin{aligned}&\left(\hat{z}-\frac{df'(x')}{dx'}\hat{x}\right)\cdot\nabla' g\\ &= \frac{i}{4\pi}\sum_{q=1}^{Q}\left(\mp\frac{df'(x')}{dx'}ik\sin\alpha_q+ik\cos\alpha_q\right)e^{-ikz\cos\alpha_q}e^{ik|x-x'|\sin\alpha_q}\Delta\alpha_q e^{ikz'\cos\alpha_q}\end{aligned} \tag{109}$$

This can also be extended to 3D problems through the following equation

$$g(\bar{r},\bar{r}') = \frac{\exp\left(ik|\bar{r}-\bar{r}'|\right)}{4\pi|\bar{r}-\bar{r}'|} = \frac{i}{8\pi}\int_{-\infty}^{\infty} dk_z e^{ik_z(z-z')}H_0^{(1)}(k_\rho|\bar{\rho}-\bar{\rho}'|) \tag{110}$$

Further (109) can be written as:

$$g\left(x,z;x',z'\right)=\frac{i}{4\pi}\sum_{q=1}^{Q}e^{ik(x-x_c)\sin\alpha_q-ikz\cos\alpha_q}e^{ik(x_c-x_{c'})\sin\alpha_q}\Delta\alpha_q e^{-ik(x'-x_c')\sin\alpha_q+ikz'\cos\alpha_q}\ \text{suppose } x>x'$$

$$g\left(x,z;x',z'\right)=\frac{i}{4\pi}\sum_{q=1}^{Q}e^{-ik(x-x_c)\sin\alpha_q-ikz\cos\alpha_q}e^{-ik(x_c-x_{c'})\sin\alpha_q}\Delta\alpha_q e^{ik(x'-x_c')\sin\alpha_q+ikz'\cos\alpha_q}\ \text{suppose } x<x'$$

(111)

In equation(111), *x*, *z*, and *x', z'* are defined on dense grid, e.g. 64 points per wavelength, while x_c and x_c' are defined on coarse grid, e.g. 8 points per wavelength. In such a case, x_c can be defined as the local patch center: x_c is the center of every 8 *x*s. Similarly for the gradient of Green function, we have

$$\left(\hat{z}-\frac{df'(x')}{dx'}\hat{x}\right)\cdot\nabla' g$$

$$=\frac{i}{4\pi}\sum_{q=1}^{Q}\left(\mp\frac{df'(x')}{dx'}ik\sin\alpha_q e^{ik|x-x'|\sin\alpha_q}+ik\cos\alpha_q e^{ik|x-x'|\sin\alpha_q}\right)e^{-ikz\cos\alpha_q}\Delta\alpha_q e^{ikz'\cos\alpha_q}$$

$$=\frac{i}{4\pi}\sum_{q=1}^{Q}e^{ik(x-x_c)\sin\alpha_q-ikz\cos\alpha_q}\left(\frac{df'(x')}{dx'}ik\sin\alpha_q e^{ik(x_c-x_{c'})\sin\alpha_q}+ik\cos\alpha_q e^{ik(x_c-x_{c'})\sin\alpha_q}\right)\Delta\alpha_q e^{-ik(x'-x_c)\sin\alpha_q+ikz'\cos\alpha_q}$$

suppose $x>x'$

$$\left(\hat{z}-\frac{df'(x')}{dx'}\hat{x}\right)\cdot\nabla' g$$

$$=\frac{i}{4\pi}\sum_{q=1}^{Q}e^{-ik(x-x_c)\sin\alpha_q-ikz\cos\alpha_q}\left(-\frac{df'(x')}{dx'}ik\sin\alpha_q e^{-ik(x_c-x_{c'})\sin\alpha_q}+ik\cos\alpha_q e^{-ik(x_c-x_{c'})\sin\alpha_q}\right)\Delta\alpha_q e^{ik(x'-x_c)\sin\alpha_q+ikz'\cos\alpha_q}$$

suppose $x<x'$

(112)

(111) and (112) are the final equations we are using for combining low rank property and fast Fourier transform. The equations are a summation of integration points from 1 to *Q*. Then we can read the equations from right to left.

For example, suppose we are doing the following multiplication

$$\sum_{n\in m_{far}} g\left(x_m,z_m;x_n,z_n\right)I_n \tag{113}$$

m_{far} denotes the far field group of field point *m* and suppose $x_m > x_n$. We can solve (114) using the following method

$$\sum_{n\in m_{far}} g\left(x_m, z_m; x_n, z_n\right) I_n = \sum_{n\in m_{far}} \frac{i}{4\pi} \sum_{q=1}^{Q} \left[e^{ik(x_m - x_{m,c})\sin\alpha_q - ikz\cos\alpha_q} \right] e^{ik(x_{m,c} - x_{n,c'})\sin\alpha_q} \left[e^{-ik(x_n - x_{n,c})\sin\alpha_q + ikz_n\cos\alpha_q} \Delta\alpha_q I_n \right] \tag{114}$$

As can be seen from equation(114), we can follow the below 3 procedures to calculate (113).

1. Dense source (64 points per wavelength) grid aggregates to the coarse grid (8 points per wavelength) for $\left[e^{-ik(x_n - x_{n,c})\sin\alpha_q + ikz_n\cos\alpha_q} \Delta\alpha_q I_n \right]$
2. Using FFT to perform the translation between interactions defined on coarse grid due to the fact that x_m, x_n are defined on conanical grid.
3. Then from coarse grid, disaggregate to dense field grid through $\left[e^{ik(x_m - x_{m,c})\sin\alpha_q - ikz\cos\alpha_q} \right]$.

In equation (111) and (112), the far field interaction of impedance matrix is decomposed into up triangular matrix and lower triangular matrix. Also identical to other fast methods, the near field interaction is calculated directly.

5.3 Results

As can be seen from equation (111) and (112), one key point is to test the convergence of the integral with different quadrature points used in the integral. This include two parts

1)how to determine *BW* which is the bandwidth

2)how to determine *Q* which is the number of points used in the quadrature

Also as illustrated in section 5.2, *BW* and *Q* are determined by x_{min} and x_{max}, respectively. But for our rough surface scattering problem, x_{min} is almost fixed, e.g., the range of near field

interaction distance like 2λ. But x_{max} could be very long, e.g., 200 λ long. In the following test, I have let *Q*=73. Then according to equation (104), we can calculate x_{min} from x_{max} or calculate x_{max} from x_{min}. Then we can know all the α points.

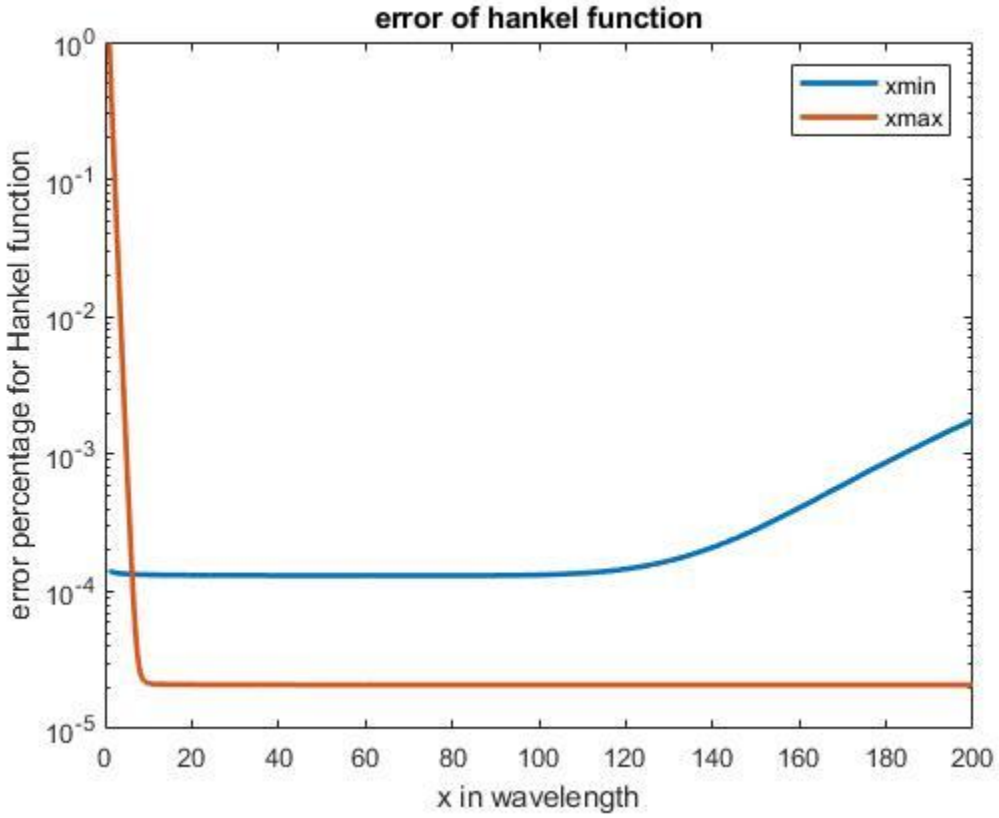

Figure 31 Error of green function calculated by steepest descent method compared to truth value

In Figure 31 we are plotting the error of green function calculated by equation (94) compared to truth value. There are two curves in the figure. As illustrated before *Q*=73, red curve denote that $x_{max} = 100\lambda$, blue curve denote that $x_{min} = 1\lambda$. It can be seen in the figure that $x_{min} = 1\lambda$ typically can make the error of green function within 0.1% difference compared to truth value for an *x* range from 0 to 140λ. Considering the fact that the largest surface length to simulate with available resource is less than 140λ, we will use the α_q points determined by *Q*=73 and $x_{min} = 1\lambda$ in the following sections.

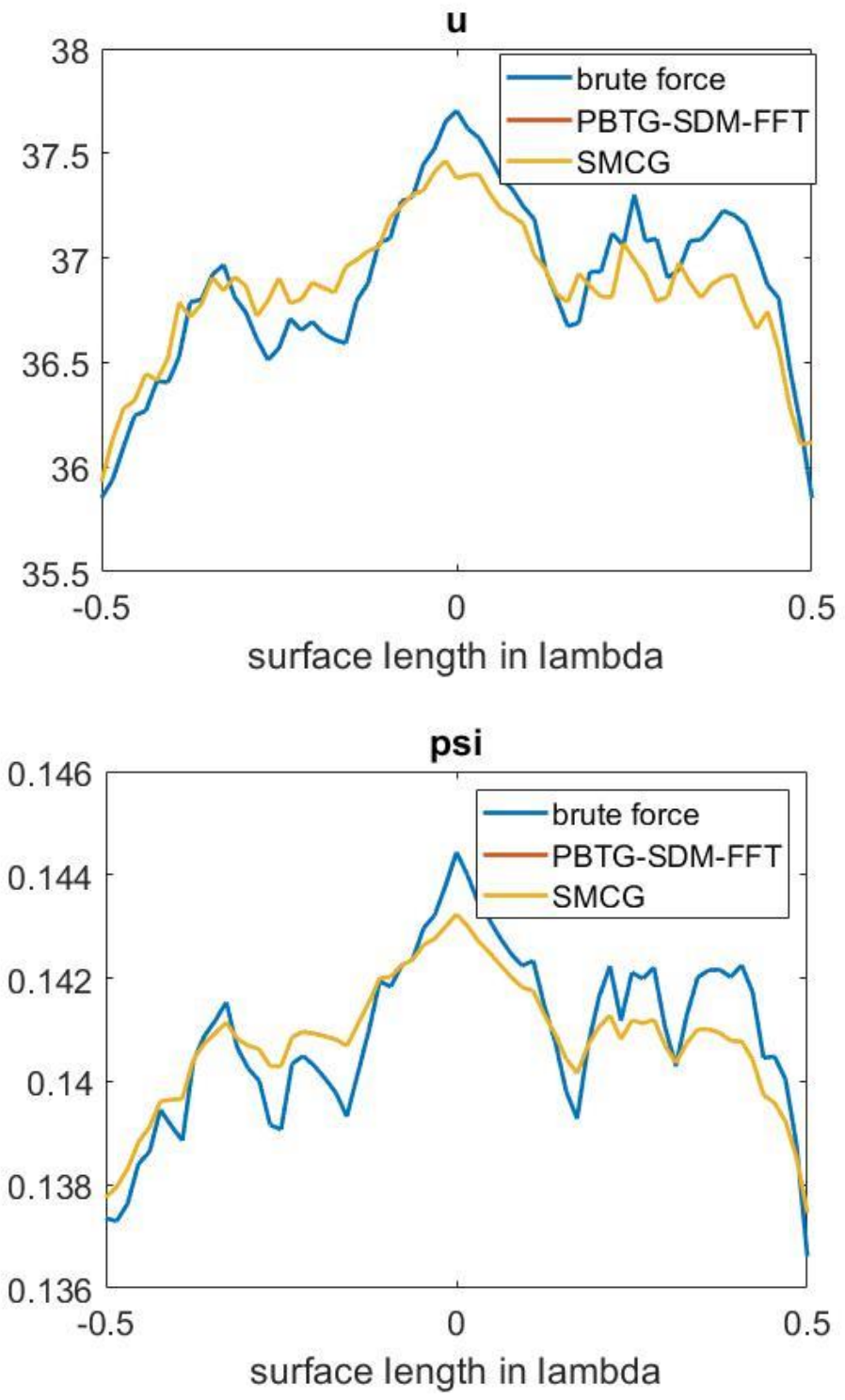

Figure 32 Surface fields comparison between SMCG, PBTG-SDM-FFT and brute force solution. Top figure is for u comparison, bottom figure is for ψ comparison.

Figure 32 shows a surface currents comparison between SMCG, PBTG-SDM-FFT method with brute force solution. The case is surface length=30λ and wind speed is 5 m/s The dense grid used is 64 points per wavelength. The coarse grid is 8 points per wavelength. The Frobenius norm error defined in (81) is used. It shows that the error norm of our proposed new method is around 0.9%.

5.4 Conclusion

In this chapter, we are showing a new method of combining SMCG method and PBTG. As is shown in chapter 4, dense grid is necessary to get correct results. At the same time dense grid is only required by lower lossy medium, but not the air green function. This chapter aims to apply dense grid to the lossy medium green function but use coarse grid to the air green function.

The novel new method exploits the steepest descent method, and finally gets to a point where dense grid is aggregated to coarse grid first then FFT can be applied. The final results show that our new method is both fast and accurate.

Chapter 6 Conclusions

Ocean surface covers approximately 70% of the Earth's surface, is dynamic on a variety of scales, and contains most of the Earth's water as well as important marine ecosystems. Remote sensing of ocean at microwave bands is of vital importance in prediction of disaster, ocean current circulation, salinity study.

This dissertation focuses on the scattering problem of ocean surfaces by numerical method. Compared to analytical method, numerical method is proven to be more accurate and involves more physical information of the real ocean geometry. Analytical method like two scale model, small slope approximation, advanced integral equation method, make approximations in the modeling process and thus have a limited range of implementations. On the numerical method sides, there are some approximations people usually made to ease the computation. One is the perfect electric conductor assumption for sea water surface. Another is the impedance boundary condition assumption. But after all, the most accurate method is just to solve the dual surface integral equation derived from Maxwell equation directly. In Chapter 2 and 3, we established the accuracy of NMM3D through comparing to the measured data.

Compared to soil surface which is usually characterized by exponential correlation function, ocean spectrum is smoother. But even for moderate wind speeds, e.g. 10 m/s, the ocean surface has an rms height as large as 1λ. This is because most power of ocean concentrates on gravity waves. This requires the simulation of a much larger surface area compared to soil surface. On the other hand, due to the large dielectric constant, dense grid is necessary to get correct results.

However, air permittivity is small and free space green function is smooth. Thus in fact, dense grid is only necessary for discretizing the green function in the medium, coarse grid is fine for free space. In Chapter 4 and 5, we proposed a novel method called NIBC to resolve the slow convergence rate issue brought by dense grid. Also, we combined SMCG and PBTG so that only coarse grid is used in the free space.

In this thesis, first of all, we have proved the accuracy of NMM3D simulations. The NMM3D results are compared to Aquarius data and is shown to have a maximum 2dB difference. Then we proposed a novel method called NIBC to alleviate the slow convergence problem brought by dense grid. Finally, a new computational method which combine SMCG and PBTG to achieve the goal that coarse grid is used in up medium while dense grid is used in lower lossy medium. Through NMM3D, we also explored the reason of NUC appeared in L band. It is concluded that at L band, Bragg scattering dominate the backscatter.

BIBLIOGRAPHY

[1] K. Fung and K. S. Chen, *Microwave Scattering and Emission Models for Users,* Norwood, MA, USA: Artech House, 2010.

[2] L. Tsang, J. A. Kong and R. T. Shin, *Theory of Microwave Remote Sensing*, Hoboken, JK, USA: Wiley, 1985.

[3] K. S. Chen, T.-D. Wu, L. Tsang, Q Li, J. Shi and A. K. Fung, "Emission of rough surfaces calculated by the integral equation method with comparison to three-dimensional moment method simulations." *IEEE Trans. Geosci. Remote Sens.*, vol. 41, no. 1, pp. 90-101, Jan. 2003.

[4] Teixeira, F. L., R. J. Burkholder, J. T. Johnson, and C. Yardim, "An efficient implementation of the nonlocal small-slope approximation for bistatic scattering from two-dimensional rough surfaces." In *Proc. USNC-URSI Radio Science Meeting*, Jun./July. 2016, pp.95-96.

[5] Guérin, Charles-Antoine, and Joel T. Johnson. "A simplified formulation for rough surface cross-polarized backscattering under the second-order small-slope approximation," *IEEE Trans. Geosci. Remote Sens.*, vol. 53, no.11, pp.6308-6314, Nov. 2015.

[6] A. Voronovich, "Small-slope approximation for electromagnetic wave scattering at a rough interface of two dielectric half-spaces."*Waves in Random Media*, vol. 4, no. 3, pp. 337-368, 1994.

[7] W. J. Plant, "A two-scale model of short wind-generated waves and scatterometry." *J. of Geophys. Res:, Oceans*, vol. 91, no. C9, pp.10735-10749, Sep. 1986.

[8] S. H. Yueh, "Modeling of wind direction signals in polarimetric sea surface brightness temperature," *IEEE Trans. Geosci. Remote Sens.*, vol. 35, no. 6, pp. 1400-1418, Nov. 1997.

[9] S. Huang, L. Tsang, E. G. Njoku, and K.S. Chen, " Backscattering coefficients, coherent reflectivities, and emissivities of randomly rough soil surfaces at L-band for SMAP applications based on numerical solutions of Maxwell equations in three-dimensional simulations, " *IEEE Trans. Geosci. Remote Sens*., vol.48, no.6, pp.2557-2568, June 2010.

[10] W. Yang, Z. Zhao, and Z. Nie, "Fast fourier transform multilevel fast multipole algorithm in rough ocean surface scattering." *Electromagnetics*, vol. 29, vol. 7, pp. 541-552, Sep. 2009.

[11] S. Huang, and L. Tsang, "Electromagnetic scattering of randomly rough soil surfaces based on numerical solutions of Maxwell equations in 3 dimensional simulations using a hybrid UV/PBTG/SMCG method," *IEEE Trans. Geosci. Remote Sens*., vol. 50, no. 10, pp. 4025-4035, Oct. 2012.

[12] T.-H. Liao , L. Tsang, S. Huang, N. Niamsuwan, S. Jaruwatanadilok, S.-B. Kim, H. Ren and K.-L Chen. "Copolarized and Cross polarized backscattering from random rough soil

surfaces from L-band to Ku-band using numerical solutions of Maxwell's equations with near-field precondition," *IEEE Trans. Geosci. Rem. Sens*., vol. 54, no. 2, pp. 651-662, Feb. 2016.

[13] J. Yang, Y. Du, and J. Shi. "Polarimetric simulations of bistatic scattering from perfectly conducting ocean surfaces with 3 m/s wind speed at L-band." *IEEE. Sel. Topics Appl. Earth Observ. Remote Sens.*, vol. 9, no. 3, pp. 1176-1186, Mar 2016.

[14] L. Tsang, J. A. Kong and R. T. Shin, *Scattering of electromagnetic waves: Numerical simulations*, vol. 2. Hoboken, NJ, USA: Wiley, 2000.

[15] J.-W. Hao, W. Song, and X.-Q. Sheng. "Efficient algorithm for calculating backscattering from two-dimensional rough sea surface under low grazing angle." in *Proc. IEEE Int. Geosci. Remote Sens. Symp. (IGARSS)*, Ju. 2016, pp.3695-3698.

[16] D. Miret, G. Soriano, F. Nouguier, P. Forget, M. Saillard, and C.-A. Guerin, "Sea surface microwave scattering at extreme grazing angle: numerical investigation of the Doppler shift." *IEEE Trans. Geosci. Remote Sens*., vol. 52, no. 11, pp. 7120-7129, Feb. 2014.

[17] G. Soriano, C.-A. Guerin, and M. Saillard, "Microwave ocean scattering at low-grazing angles with the GMOM." *Radar Conference (EuRAD), European IEEE*, pp. 5-8, 2010.

[18] P. Spiga, G. Soriano, and M. Saillard, "Scattering of electromagnetic waves from rough surfaces: a boundary integral method for low-grazing angles." *IEEE Trans. Geosci. Remote Sens.*, vol. 56, no. 7, pp. 2043-2050, Jul. 2008.

[19] J. T. Johnson, R. T. Shin, J. A. Kong, L. Tsang, and K. Pak, "A numerical study of the composite surface model for ocean backscattering." *IEEE Trans. Geosci. Remote Sens*., vol. 36, no. 1, pp. 72-83, Jan. 1998.

[20] Q. Li, C. H. Chan, L. Tsang, and G. Zhang, "Wave scattering from a lossy dielectric rough suface using PBTG BMIA/CAG and applications to passive remote sensing." In *Geoscience and Remote Sensing Symposium Proceedings*, 1998. IGARSS'98. 1998 IEEE International (Vol. 3, pp. 1469-1471). IEEE.

[21] D. Miret, G. Soriano, and M. Saillard, "Rigorous simulations of microwave scattering from conductivity two-dimensional sea surfaces at low grazing angles." *IEEE Trans. Geosci. Remote Sens*., vol. 52, no. 6, pp. 3150-3158, Jun. 2014.

[22] S. Q. Li, C. H. Chan, L. Tsang, Q. Li, and L. Zhou, "Parallel implementation of the sparse matrix/canonical grid method for the analysis of two-dimensional random rough surface (three-dimensional scattering problem) on a beowulf system," *IEEE Trans. Geosci. Remote Sens*., vol. 38, no. 4, pp.1600-1608, July, 2000.

[23] S. H. Yueh, W. J. Wilson and S. Dinardo, "Polarimetric radar remote sensing of ocean surface wind," *IEEE Trans. Geosci. Remote Sens*., vol. 40, no. 4, pp.793-800, April 2002.

[24] S. P. Durden and J. F. Vesecky, "A physical radar cross-section model for a wind-driven sea with swell," *IEEE J. Oceanic Eng*., vol. OE-10, pp. 445-451, Oct. 1985.

[25] N. Pinel, B. Chapron, C. Bourlier, N. de Beaucoudrey, R. Garello and A. Ghaleb, "Statistical analysis of Real Aperture Radar field backscattered from sea surfaces under moderate winds by Monte Carlo simulations," *IEEE Trans. Geosci. Remote Sens*., vol. 52, no. 10, pp.6459-6470, Oct. 2014.

[26] T. Elfouhaily, B. Chapron, K. Katsaros and D. Vandemark, “A unified directional spectrum for long and short wind-driven waves,” *Journal of Geophysical Research*, vol. 102. no. c7, pp. 15781-15796, July 15, 1997.

[27] F. Nouguier, C. A. Guérin, and B. Chapron. "Choppy wave” model for nonlinear gravity waves." *Journal of Geophysical Research*, vol. 114, no. C09012, Sep. 2009.

[28] A. K. Fung, *Backscattering from multiscale rough surfaces with application to wind scatterometry*, Artech House, 2015.

[29] H. Braunisch, Y. Zhang, C.O. Ao, S.E. Shih, Y.C. E. Yang, K.H. Ding, J.A. Kong and L. Tsang, "Tapered Wave with Dominant Polarization State for All Angles of Incidence," *IEEE Transactions on Antennas and Propagation*, vol. 48, no. 7, pp1086-1096, July 2000.

[30] A. G. Voronovich and U. Z. Valery, "Sensitivity of modeled polarimetric radar ocean scattering to wind direction," *IEEE Geoscience and Remote Sensing Symposium (IGARSS)*, 2014.

[31] P. A. Hwang, and D. W. Wang. "An empirical investigation of source term balance of small scale surface waves." *Geophysical Research Letters*, vol. 31, L15301, Aug. 2004.

[32] Y. Liu., M.Y. Su, X. H. Yan and W. T. Liu, “The mean-square slope of ocean surface waves and its effects on radar backscatter*,” Journal of atmospheric and oceanic technology*, vol. 17, pp.1092-1105, Aug. 2000.

[33] C. Cox and W. Munk, “Statistics of the sea surface derived from sun glitter,” *Journal of Marine Research*, 13(2), 198-227, 1954.

[34] J. W. Wright, “A new model for sea clutter,” *IEEE Transactions on Antennas and Propagation*, vol. 16, no. 2, pp.217-223, 1968.

[35] O. Isoguchi and M. Shimada, “An L-band ocean geophysical model function derived from PALSAR,” *IEEE Trans. Geosci. Remote Sens*., vol. 47, no. 7, pp. 1925-1936, July 2009.

[36] M. V. Yurovskaya, V. A. Dulov, B. Chapron and V. N. Kudryavtsev, “Directional short wind wave spectra derived from the sea surface photography,” *Journal of Geophysical Research*, vol. 118, pp. 4380-4394, Sep. 2013.

[37] J. T. Johnson, L. Tsang, R. T. Shin, K. Pak, C. H. Chan, A. Ishimaru, and Y. Kuga. "Backscattering enhancement of electromagnetic waves from two-dimensional perfectly conducting random rough surfaces: A comparison of Monte Carlo simulations with experimental data." *IEEE Transactions on Antennas and Propagation*, vol. 44, no. 5, pp. 748-756, May. 1996.

[38] S. H. Yueh, W. Tang, A. G. Fore, G. Neumann, A. Hayashi, A. Freedman, J. Chaubell, and G. Lagerloef. "L-band passive and active microwave geophysical model functions of ocean surface winds and applications to Aquarius retrieval." *IEEE Trans. Geosci. Remote Sens*., vol. 51, no. 9, pp. 4619-4632, Sep. 2013.

[39] Z. Zhao, and J. C. West. "Low-grazing-angle microwave scattering from a three-dimensional spilling breaker crest: A numerical investigation." *IEEE Trans. Geosci. Remote Sens*., vol. 43, no. 2, pp. 286-294, Feb. 2005.

[40] D. R. Thompson., T. M. Elfouhaily, and J. L. Garrison. "An improved geometrical optics model for bistatic GPS scattering from the ocean surface." *IEEE Transactions on Geoscience and Remote Sensing* 43.12 (2005): 2810-2821.

[41] Johnson, J. T., & Chou, H. T. (1998, July). Numerical studies of low grazing angle backscatter from 1D and 2D impedance surfaces. In *Geoscience and Remote Sensing Symposium Proceedings, 1998. IGARSS'98*. 1998 IEEE International (Vol. 4, pp. 2295-2297). IEEE.

[42] V. I. Shrira, S. I. Badulin, and C. Kharif, "A model of water wave 'horse-shoe'patterns." *Journal of Fluid Mechanics*, vol. 318, pp. 375-405, 1996.

[43] Y. Du, X. Yang, K.-S. Chen, W. Ma, Z. Li, "An improved spectrum model for sea surface radar backscattering at L-Band," *Remote Sens*., vol 9, page 776, 2017.

[44] T. Qiao, L. Tsang, D. Vandemark, S. H. Yueh, T.-H. Liao, F. Nouguier, and B. Chapron. "Sea Surface Radar Scattering at L-Band Based on Numerical Solution of Maxwell's Equations in 3-D (NMM3D)." *IEEE Trans. Geosci. Remote Sens.*, accepted, 2018.

[45] N. Reul, J. Tenerelli, B. Chapron, D. Vandemark, Y. Quilfen, and Y. Kerr. "SMOS satellite L-band radiometer: A new capability for ocean surface remote sensing in hurricanes." *Journal of Geophysical Research: Oceans* 117, no. C2, 2012.

[46] S. Huang, L. Tsang, E. G. Njoku, and K-S. Chan. "Backscattering coefficients, coherent reflectivities, and emissivities of randomly rough soil surfaces at L-band for SMAP applications based on numerical solutions of Maxwell equations in three-dimensional simulations." *IEEE Trans. Geosci. Remote Sens.*, vol. 48, no. 6, pp. 2557-2568, 2010

[47] T. Qiao, L. Tsang, and S. Tan. "Scattering of lossy dielectric surfaces in full wave simulation of Maxwell's equations with dense grid and neighborhood impedance boundary conditions." In *Progress in Electromagnetics Research Symposium-Fall (PIERS-FALL)*, 2017, pp. 3054-3057. *IEEE*, 2017.

[48] Q. Li, and L. Tsang. "Wave scattering from lossy dielectric random rough surfaces using the physics-based two-grid method in conjunction with the multilevel fast multipole method." *Radio Science*, vol. 36, no. 4, pp. 571-583, 2001.

[49] L. Tsang, J. A. Kong and R. T. Shin, *Scattering of electromagnetic waves: Theories and applications*, vol. 1, John Wiley & Sons, 2000.

[50] T. Qiao, Y. Du, L. Tsang, "Electromagnetic scattering and emission by ocean surfaces based on neighborhood impedance boundary condition (NIBC) with dense grid: accurate emissivity and sensitivity to salinity," submitted to *Progress in Electromagnetic Research (PIER)*, 2018.